FEDERAL INSTITUTE OF EDUCATION, SCIENCE AND TECHNOLOGY OF SANTA CATARINA – CÂMPUS FLORIANÓPOLIS
ACADEMIC DEPARTMENT OF ELECTROTECHNICS
BACHELOR'S DEGREE PROGRAM IN ELECTRICAL ENGINEERING

JOÃO VITOR RUSSI BENEDET

SIMULATION AND CORRECTIVE MAINTENANCE TRIALS OF WORM DRIVES IN PITCH CONTROL SYSTEMS: a proof of concept considering track position and thermal expansion through laser additive manufacturing

FLORIANÓPOLIS, 2025.

FEDERAL INSTITUTE OF EDUCATION, SCIENCE AND TECHNOLOGY OF SANTA CATARINA – CÂMPUS FLORIANÓPOLIS
ACADEMIC DEPARTMENT OF ELECTROTECHNICS
BACHELOR'S DEGREE PROGRAM IN ELECTRICAL ENGINEERING

JOÃO VITOR RUSSI BENEDET

SIMULATION AND CORRECTIVE MAINTENANCE TRIALS OF WORM DRIVES IN PITCH CONTROL SYSTEMS: a proof of concept considering track position and thermal expansion through laser additive manufacturing

Final Course Thesis submitted to the Federal Institute of Education, Science and Technology of Santa Catarina as part of the requirements for obtaining the degree of Electrical Engineer in 2025.

Advisor:
Prof. Everthon Taghori Sica, D. Ing.

Co-Advisor:
Rebar Hama-Saleh, M. Ing.

FLORIANÓPOLIS, 2025.

Ficha de identificação da obra elaborada pelo autor.

Benedet, João Vitor
Simulation and corrective maintenance trials of worm drives in pitch control systems: a proof of concept considering track position and thermal expansion through laser additive manufacturing / João Vitor Benedet; orientação de Everthon Sica; coorientação de Rebar Hama-Saleh. - Florianópolis, SC, 2025.
76 p.
Trabalho de Conclusão de Curso (TCC) - Instituto Federal de Santa Catarina, Câmpus Florianópolis. Bacharelado em Engenharia Elétrica. Departamento Acadêmico de Eletrotécnica.
Inclui Referências.

1. Sistemas de controle de pitch. 2. Deposição de Material a Laser (LMD). 3. Sensores à Laser. 4. Detecção de bordas em nuvem de pontos. I. Sica, Everthon. II. Hama-Saleh, Rebar. III. Instituto Federal de Santa Catarina. IV. Simulation and corrective maintenance trials of worm drives in pitch control systems.

SIMULATION AND CORRECTIVE MAINTENANCE TRIALS OF WORM DRIVES IN PITCH CONTROL SYSTEMS: a proof of concept considering track position and thermal expansion through laser additive manufacturing

JOÃO VITOR RUSSI BENEDET

This work has been judged suitable for obtaining a bachelor's degree in electrical engineering and approved in its final form by the evaluation committee of the Electrical engineering Course at the Federal Institute of Education, Science and Technology of Santa Catarina.

Aachen, 2025.

Evaluation committee members:

Documento assinado digitalmente
gov.br
EVERTHON TAGHORI SICA
Data: 25/07/2025 11:47:31-0300
Verifique em https://validar.iti.gov.br

Everthon Taghori Sica, D. Ing.
IFSC Florianópolis (Advisor)

Rebar Hama-Saleh Abdullah
Digital unterschrieben von Rebar Hama-Saleh Abdullah
Datum: 2025.07.28 10:20:11 +02'00'

Rebar Hama-Saleh, M. Ing.
Fraunhofer ILT (Co-Advisor)

Documento assinado digitalmente
gov.br
ERWIN WERNER TEICHMANN
Data: 28/07/2025 11:28:13-0300
Verifique em https://validar.iti.gov.br

Erwin Werner Teichmann, D. Ing.
IFSC Florianópolis

Documento assinado digitalmente
gov.br
SERGIO LUCIANO AVILA
Data: 28/07/2025 11:45:05-0300
Verifique em https://validar.iti.gov.br

Sérgio Luciano Avila, D. Ing.
IFSC Florianópolis

ACKNOWLEDGEMENTS

I would like to thank and express my utmost gratitude to the two most important people in the world: my mother, Lilian Meri Russi Benedet, and my father, Gilmar Benedet, who have guided me every day to become who I am and who I strive to be. I also thank my brother, Gian Carlo Benedet, who inspired me to study and pursue a career in engineering, and my sister, Bianca Benedet, whom I miss very much and hope to see soon in the US. I would also like to thank my partner, Eduarda Cordeiro, who chose to embark on this Germanic journey with me and supports me every single day.

I am also deeply grateful to my two advisors for this work, Professor Everthon Taghori Sica and Rebar Hama-Saleh, who did everything they could to support both this project and my stay in Germany. I also thank Professor Erwin Werner Teichmann, who made this international experience possible, and Professor Sérgio Luciano Avila, who helped me be ready for this opportunity through my internship at PECCE-IFSC.

Lastly, I extend my thanks to the friends I have made both here at the ILT and at IFSC, who have supported me warmly along the way.

ABSTRACT

Wind power has become a cornerstone of sustainable development strategies. Among the key components ensuring wind turbine reliability, pitch control systems are particularly prone to failure, largely due to the harsh operational conditions they endure, especially within their gear mechanisms, such as worm drives. These conditions accelerate wear and failure, demanding advanced maintenance and repair strategies. This study investigates the potential of Laser Material Deposition (LMD) as a remanufacturing technique for worm drives and proposes a sensor-aided system to detect and correct geometric misalignments that arise from thermal expansion during the process. The work includes hardware integration, surface treatment evaluation, and script development. Using a high-speed 2D profile scanner integrated into a Computer Numeric Control (CNC) machine, various scanning trials were conducted under different surface treatments and at two scanning speeds. The study demonstrates the feasibility of integrating laser scanning and real-time data processing for geometry correction in LMD. By improving accuracy and reducing reliance on post-processing or operator intervention, this approach lays the groundwork for closed-loop geometry control systems in additive manufacturing.

Keywords: Pitch control systems. Laser Material Deposition (LMD). Laser-based Sensors. Point-cloud edge detection.

RESUMO

A energia eólica tornou-se um pilar central das estratégias de desenvolvimento sustentável. Entre os principais componentes que garantem a confiabilidade das turbinas eólicas, os sistemas de controle de pitch são especialmente suscetíveis a falhas, principalmente devido às severas condições operacionais a que são submetidos, especialmente, em seus mecanismos de engrenagem, como as engrenagens sem-fim. Essas condições aceleram o desgaste e as falhas, exigindo estratégias avançadas de manutenção e reparo. Este estudo investiga o potencial da Deposição de Material a Laser (LMD) como técnica de remanufatura para engrenagens sem-fim e propõe um sistema assistido por sensor para detectar desalinhamentos geométricos provocados pela expansão térmica durante o processo. O trabalho inclui integração de hardware, avaliação de diferentes superfícies e desenvolvimento de scripts. Utilizando um scanner de perfil 2D de alta velocidade integrado a uma máquina Comando Numérico Computadorizado (CNC), foram realizados diversos testes de varredura com diferentes tratamentos de superfície e em duas velocidades de escaneamento. O estudo demonstra a viabilidade de integrar escaneamento a laser e processamento de dados em tempo real para correção geométrica em processos de LMD. Ao melhorar a precisão e reduzir a dependência de pós-processamento ou intervenção do operador, essa abordagem estabelece as bases para sistemas de controle da geometria em malha fechada na manufatura aditiva.

Palavras-chave: Sistemas de controle de *pitch*. Deposição de Material a Laser (LMD). Sensores à Laser. Detecção de bordas em nuvem de pontos.

LIST OF FIGURES

LIST OF TABLES

LIST OF ABBREVIATIONS AND ACRONYMS

CNC	Computer Numeric Control
CSV	Comma Separated Value
CTE	Coefficient of Thermal Expansion
DED	Direct Energy Deposition
DLL	Dynamic Link Library
EU	European Union
GIL	Global Interpreter Lock
ISE	Fraunhofer Institut für Solare Energiesysteme
ILT	Fraunhofer Institut für Lasertechnik
LAM	Laser Additive Manufacturing
LMD	Laser Material Deposition
ONS	National System Operator (Operador Nacional do Sistema)
OPC UA	Open Platform Communication Unified Architecture
PID	Proportional-Integral-Derivative
RANSAC	Random Sample Consensus
SDK	Software Development Kit

CONTENTS

1 INTRODUCTION

Given the crucial role of energy for populational and economic growth in the modern age, it is essential for that demand to be supported through this everlasting increase. Therefore, energy generation and distribution must evolve in an integrated manner to keep up with this growth (Adebayo*, et al.*, 2021). With the energy expansion, renewable alternatives gain strength as way to diverse the energy matrix, as well as to combat climate change, with over 130 countries aiming for carbon neutrality by 2050, including the European Union (EU) (Dong*, et al.*, 2022). Due to these reasons, wind power has become a central topic in debates on green energy around the world.

Historically, Brazil's energy matrix has heavily relied on hydropower, which currently accounts for over 45 % of the total installed capacity, as can be seen in Figure 1, according to the National System Operator (ONS, 2025). This brings issues to the Brazilian electric system due to the dependency in that power source, leading to risks of power outage in periods of drought, caused in parts, by climate change. Because of that, planning has shifted towards a more diverse energy matrix, while keeping it clean and renewable, with wind power being a great candidate, transforming the old hydro-thermal energetic system into a hydro-thermal-wind. In January 2025, Brazil's wind power generation reached nearly 33 GW (ONS, 2025). Additionally, plans are in place to construct over 230 GW of offshore wind capacity along the country's coastline within the next decades (Telles, 2024).

Figure 1 – Brazilian energy matrix by source in January 2025

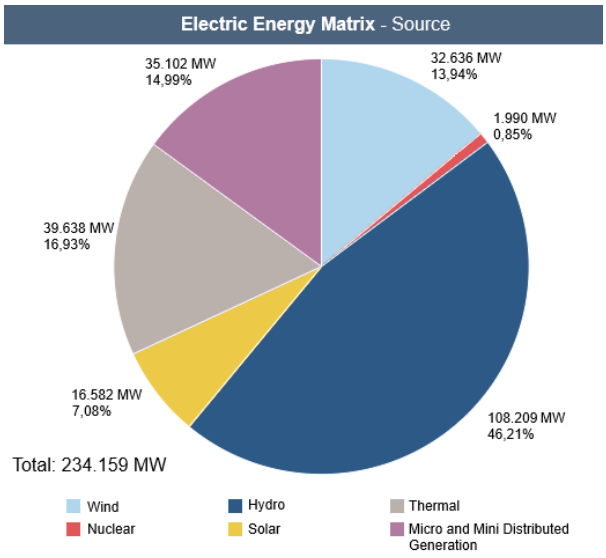

Source: Adapted from ONS (2025).

The history in Germany is different, as there was a great shift in the last 40 years from oil and coal towards a more diverse matrix, being one of the pioneers in tackling environmental issues (Adedoyin*, et al.*, 2023). In Figure 2, provided by Fraunhofer Institut für Solare Energiesysteme (Fraunhofer ISE, 2025), it can be seen the focus shift of the country on wind and solar power, as both sources lead in net installed capacity. A great majority of the wind plants in Germany are built onshore, as Figure 2 also shows, with the country's government planning to install 70 GW worth of offshore wind farms until 2045 (Bundesregierung, 2025; Whermann, 2018).

Figure 2 – German energy matrix by source in 2024

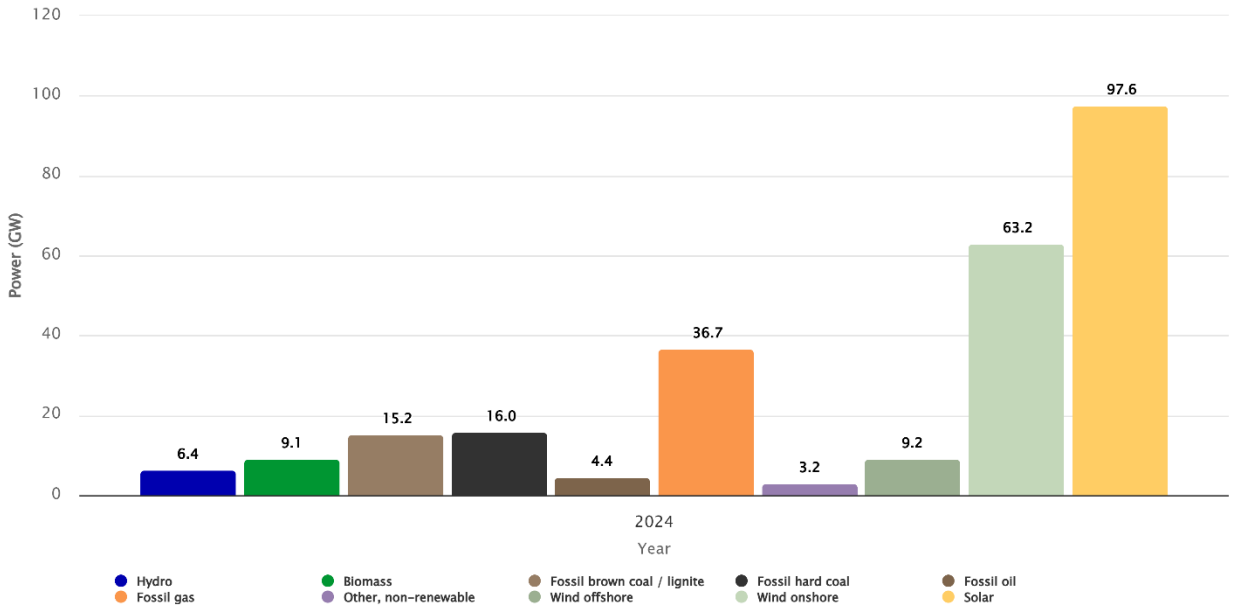

Source: Adapted from Fraunhofer ISE (2025).

This focus on wind power from both countries and others across the world brings different concerns, as one of the intrinsic difficulties of wind turbines is brought by the environment in which they are installed, being onshore or offshore, with often locations immersed in strong corrosion (offshore), high humidity, sudden climate changes, among other conditions (Nie; Wang, 2013). With that, turbines are subject to various failures, found in different parts, like the main structure, the generator, or primarily, in their gearboxes (Su*, et al.*, 2024). The nacelle, which is the name of the structure that supports the internal parts of the wind turbine, represented in Figure 3, houses gearboxes used to regulate various movement characteristics such as, for example, yaw and pitch systems. Although the nacelle is built to endure strong

corrosion especially in offshore turbines, other problems such as wear, fatigue, or excessive loading failures can be found in its gear systems, leading to efficiency reduction (Bharatbhai, 2015).

Figure 3 – Nacelle inside view

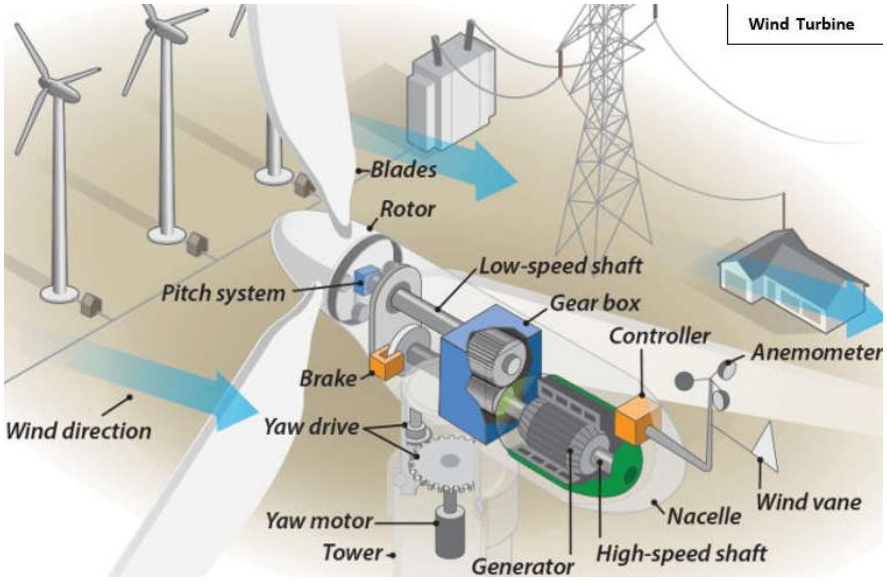

Source: Emexidis; Gkonis (2024).

Maintenance for these mentioned components in Figure 3 can be categorized into three major types: corrective, involving the repair or replacement of parts after a failure has occurred; preventive, which consists of scheduled maintenance performed at regular intervals without prior diagnostics; and predictive, which relies on periodic inspections and data analysis to detect potential failures before they occur (Koerich, 2021).

1.1 Justifications

Wind turbines generate electric energy by transforming the kinetic energy from wind velocity and density from the region (Machado, 2022). Figure 4 shows the air flow between wind blades according to the blades' models.

Figure 4 – Air flow between wind blades

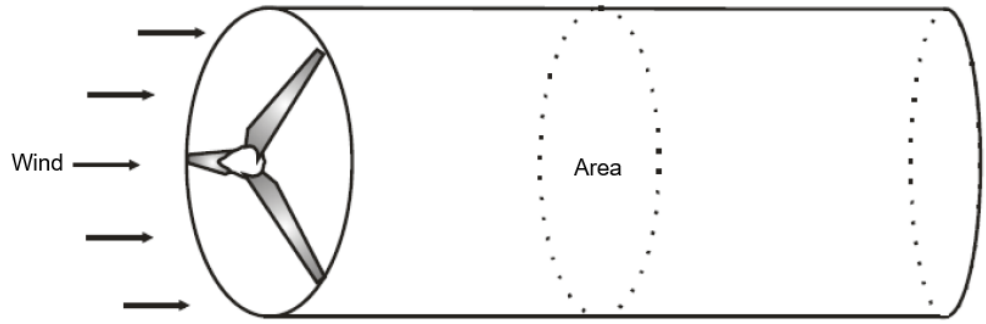

Source: Adapted from Barros (2015).

Equation 1 describes the kinetic energy shown in Figure 3 (Barros, 2015).

$$E = 0{,}5 \cdot \rho \cdot A \cdot v_w^3 \cdot t \quad (1)$$

Where ρ is the air density, A is the blade's area sweep, v_w is the wind velocity, and t is time. Also, the maximum potency which can be extracted depending on the wind velocity and the blade area sweep can be seen in Equation 2 (Barros, 2015).

$$P_m = 0{,}5 \cdot [\rho \cdot A \cdot C_p(\lambda, \beta) \cdot v^3] \quad (2)$$

Where ρ is the air density, A is the blade's area sweep, C_p is the power coefficient, λ is the ratio of the blade tip speed, β is the pitch angle and v is the wind velocity. Due to the coefficient of power (C_p), the maximum kinetic energy available from the wind does not generate the maximum possible power, with it being only a fraction of the wind power that can be extracted by the rotor (Barros, 2015; Machado, 2022).

The coefficient of power can be expressed as a function of the velocity ratio of the wind and the blade inclination angle, as indicated in Equation 3 (Machado, 2022).

$$C_p(\lambda, \beta) = 0{,}5 \cdot \left(\frac{116}{\lambda_i} - 0{,}4 \cdot \beta - 5\right) e^{\frac{-21}{\lambda}} + 0{,}0068 \cdot \lambda \quad (3)$$

Where C_p is the coefficient of power, λ is the ratio of the blade tip speed, β is the pitch angle and λ_i is an intermediate variable between λ and β, known as specific velocity, as shown in Equation 4 (Machado, 2022).

$$\lambda_i^{-1} = \frac{1}{\lambda + 0{,}08\beta} - \frac{0{,}0035}{1 + \beta^3} \quad (4)$$

It can be concluded that the power coefficient determines the amount of power that can be extracted for each wind speed impacting each angle of attack of the wind to the rotor blades (Machado, 2022). This relationship can be seen in Figure 5.

Figure 5 – Relationship between power coefficients for each inclination angle

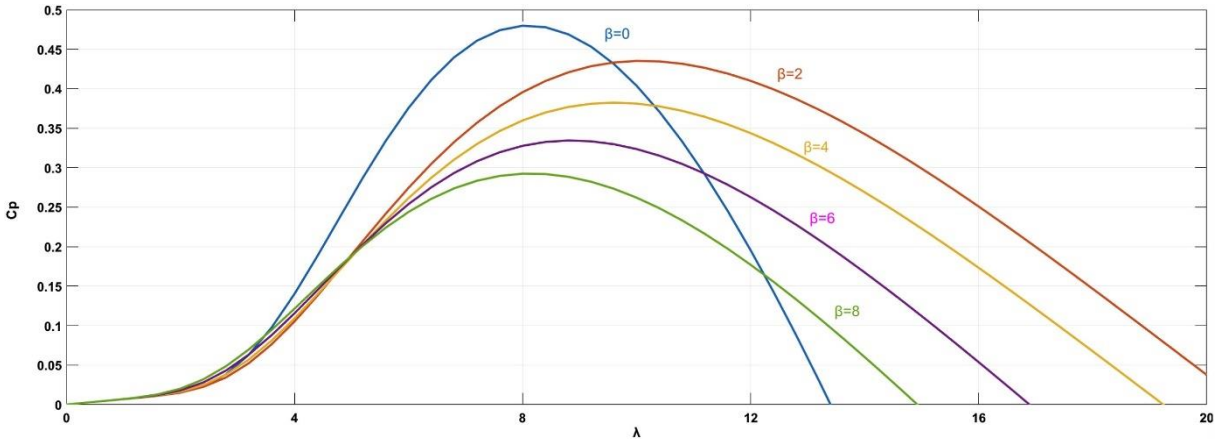

Source: Pan; Wang (2020)

In Figure 5 it is noted that the power coefficient reaches its highest efficiency at pitch angles close to zero, typically occurring under lower wind speeds, leading to no need of adjustments done to the blade pitch. As wind speed increases, the tip speed ratio (λ) also rises, resulting in a gradual increase in the blade pitch angle and decreasing the power coefficient (C_p) maintaining safe operation of the turbine. When the wind speed exceeds the rated value, it becomes necessary to take the wind turbine out of operation to prevent damage.

Yaw and pitch systems are crucial for efficient energy production from wind generators, employing the criteria discussed. The yaw system is responsible to direct the wind blades towards the wind direction by rotating the nacelle around the rotor axis, increasing the potential generated energy by the turbine (Song*, et al.*, 2019). The pitch system is the mechanism that rotates the blades to optimize the angle of attack of the wind (Kang*, et al.*, 2017). Both systems' movement can be seen in Figure 6.

Figure 6 – Yaw and pitch movements

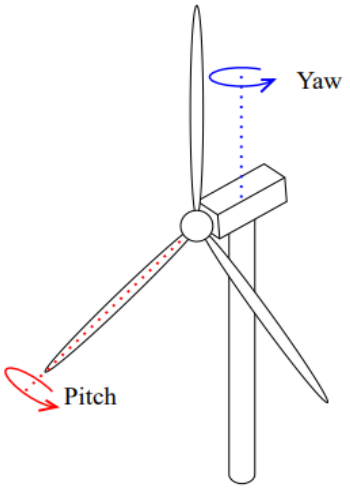

Source: Shin; Rüttgers; Lee (2022).

The pitch system also reduces the wind-related damage to the overall equipment. However, due to the extreme conditions it often faces, failures can occur. When this happens, production efficiency is reduced, potentially causing damage to the machine and resulting in downtime (Qin; Tao; Zhao, 2023). In gearboxes, most common failure modes are fatigue, wear or plastic deformation, with tooth bending fatigue being the biggest cause (Qiu*, et al.*, 2017). Pitch control systems can be built with electric drives and hydraulic drives, with the former being most common due to hydraulic systems' oil leakage and maintenance issues (Wei; Qian; Zareipour, 2020). Different drives and configurations were and are employed, such as worm-based, (Augustyn, 2020; Ha, 2020; Komass, 2016; Nagai; Ameku; Roy, 2009). Figure 7 illustrates a pitch system schematic from manufacturer "Pengky" with a worm drive present (Pengky, 2019b).

Figure 7 – Pitch system from manufacturer Pengky

Source: Pengky (2019b).

Due to their exposed position, electric pitch gears are often the first components to be affected by the wind. It is important that the worm drive has a long service life and allows for quick maintenance when necessary, in order to maximize energy production, with overall operational and maintenance costs reaching 3 % of the initial plant investment (Bianchini*, et al.*, 2022).

1.2 Problem Definition

Worm gearboxes, apart from wind turbine pitch systems, are also frequently used for power and motion transmission in industrial areas, as well as steering systems (Kim, 2018). Known for their lightweight design, they can handle high-power applications. Common failures arise from fatigue, wear, and tooth breakage (Karabacak; Gürsel Özmen; Gümüşel, 2022). Advantages of worm gearboxes include their compact size, simple configuration, low backlash, quiet operation, and damage tolerance. However they do present a lower efficiency compared to other types of gears (Elasha*, et al.*, 2014). Under harsh conditions and operating for longs periods of time, gearboxes' performances may decrease over time, needing maintenance (Karabacak; Baş, 2022). With wind turbines gearboxes developing a multitude of failures over time, good analysis and quick maintenance must be considered when managing them, especially with offshore towers, as they can be inaccessible for several months (Artigao*, et al.*, 2018). Currently, the repair process of drives requires special equipment and highly qualified personnel, increasing overall maintenance cost (Kononenko; Ignatkin; Drozdov, 2022).

One solution towards diminishing cost and time of maintenance could be Laser Additive Manufacturing (LAM), which is a technique that utilizes a laser beam to melt and solidify metal powder material into a substrate (Gong*, et al.*, 2021). Although LAM requires costly special equipment, it is a technique with a wide variety of applications, including metal coating and welding (Das; Nandan; Pandey, 2022; Fang*, et al.*, 2016; Mahmood*, et al.*, 2021). LAM can be used to counter corrosion effects as well, creating, little to no residual material waste and being more efficient than usual processes (Biserova-Tahchieva*, et al.*, 2023; Faludi*, et al.*, 2015) .

According to the American Society for Testing and Materials (2012), there are 7 main categories of Additive Manufacturing (AM): photopolymer vat, material

extrusion, powder-bed fusion, sheet lamination, binder jetting, material jetting, and directed energy deposition (DED) (Ransikarbum; Pitakaso; Kim, 2020). In DED, multiple techniques and heat sources can be employed to deposit thin layers of material, either in powder or wire form. Among these, Laser Material Deposition (LMD) has received great attention from researchers for enhancing design flexibility, serving as an alternative for constructing complex and custom geometries while reducing production cost (Donadello*, et al.*, 2019). Figure 8 shows a diagram of the LMD process, with powder-based deposition and Argon as shielding gas.

Figure 8 – Diagram of laser material deposition process

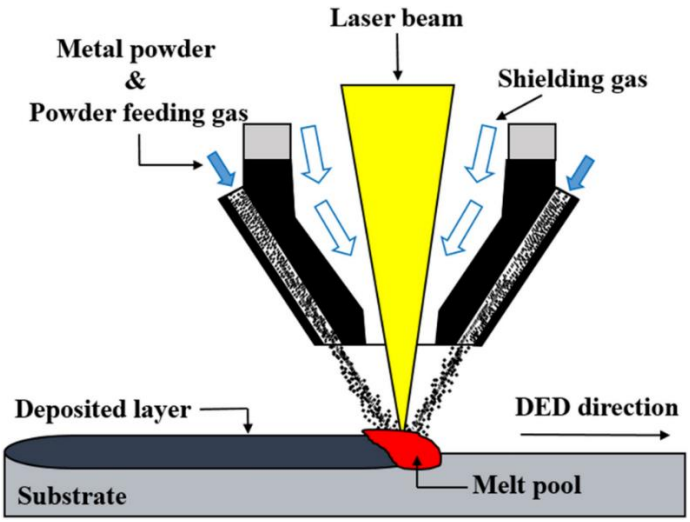

Source: Lim*, et al.* (2021).

With LMD being a multi-parameter, nonlinear, stochastic system (Gunasegaram*, et al.*, 2024), it brings multiple variables to the table, such as laser power, powder flow rate, shielding gas flow rate, temperature expansion, among others (Hu; Kovacevic, 2003a). Optimizing these parameters in a post-process environment is often time-consuming and inefficient (Cai*, et al.*, 2023; Chen*, et al.*, 2024). Making these adjustments mid-process is ideal due to reducing setup time and the need for operator expertise (Fox*, et al.*, 1998), with authors in the literature commonly focusing on only one variable to control (Cai*, et al.*, 2023). Most studies focus on analyzing the melt pool formed when the laser interacts with the metal powder, with some checking its temperature (Song*, et al.*, 2012) or width (Akbari; Kovacevic, 2019), using machine learning techniques (Scime; Beuth, 2019). With the aid of sensors, other variables were also used for controlling purposes, like powder rate (Hu; Kovacevic, 2003b), and clad

height (Toyserkani; Khajepour, 2006). Although, the quality of data gathered is essential for a good control process.

Using lasers introduces a rapid cooling and heating process in the system, which can create significant temperature gradients (Qi*, et al.*, 2020). Typically, the metal powder and substrate possess different thermophysical parameters, such as their thermal expansion coefficient, causing residual stress, generating cracks and unevenness in the laser coating (Lee*, et al.*, 2015). This unevenness can provoke a disparity between the programmed path with actual track position, resulting in accumulated errors over time and affect the near-net-shape accuracy of the cladding. Figure 9 illustrates this issue.

Figure 9 - Programmed track position alignment with actual track position and possible corrections

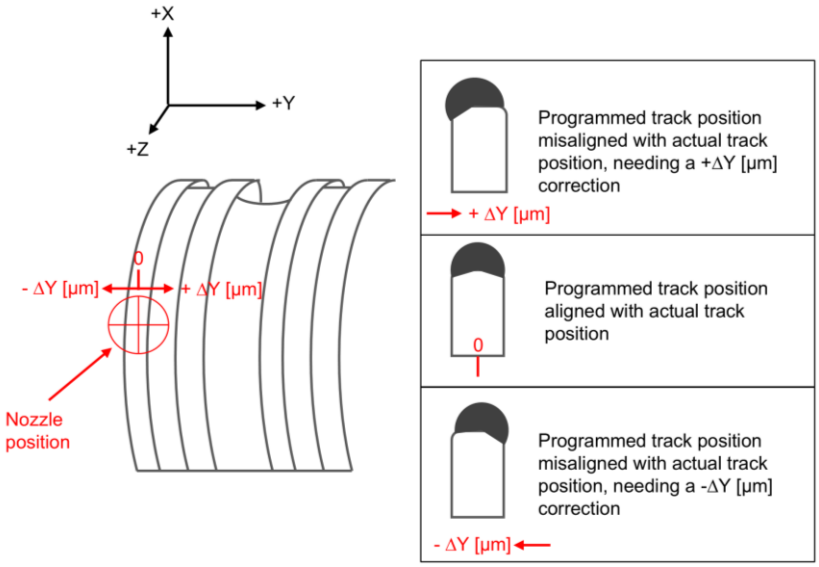

Source: Own (2025) and Fraunhofer ILT (2025).

As can be observed in Figure 9, the error caused by thermal expansion from the laser heat can result in deviations along the Y-axis during deposition, requiring either positive or negative corrections.

1.3 General Objective

The aim of this work is, with the aid of a sensor during the LMD process, promote proof of concept of a closed-loop correction of the misalignment between the

programmed path with actual track position, provoked due to thermal expansion. The subject of this study is worm drives, found in wind turbine pitch control systems.

1.4 Specific Objectives

The specific objectives are listed below:

a) Present commonly used pitch control systems, its gearboxes and worm drives;

b) Present LAM parameters, such as thermal expansion;

c) Display state-of-the-art sensor-aided control employed in the literature for geometry correction;

d) Model the proposed solution for gathering trial data and simulation;

e) Implement a code to gather data from each trial aided by the sensor and a C++ written software;

f) Implement a simulation code for fetched data using python;

g) Test different edge detection approaches for each individual trial using python;

h) Display and discuss achieved results.

1.5 Work Structure

This work is structured as follows. Chapter 2 provides an overview of various wind turbine pitch control systems, the selected maintenance approach, laser additive manufacturing and its parameters, as well as relevant sensor-aided control strategies. Chapter 3 details the modeling and implementation of the proposed solution and its trials, outlining each step undertaken in the study. Chapter 4 presents the results obtained from the techniques applied in gathered data. Finally, Chapter 5 offers concluding remarks and suggestions for future work.

2 MAINTENANCE OF WORM DRIVES IN PITCH CONTROL

As offshore wind installations continue to expand globally to meet rising renewable energy demands, the reliability of critical subsystems like the pitch control mechanism becomes increasingly important. Worm drives, often employed in pitch systems due to their self-locking ability and compact design, are subjected to harsh operational conditions that can lead to wear, fatigue, and eventual failure. Consequently, this chapter explores the fundamental aspects of pitch systems, common failure modes associated with worm drives, and emerging maintenance and repair techniques, including advanced laser additive manufacturing solutions, to enhance durability, reduce downtime, and improve cost-efficiency in offshore wind turbine operations.

2.1 Wind Turbine Pitch Control Systems

Offshore wind turbines have been getting attention all over the world, increasing its installed capacity faster than ever, with key wind players like China, United States, Brazil, India and the EU breaking annual records every year (Global Wind Energy Council, 2024). Although, to meet the COP28 targets, a climate change conference attended by over 190 nations, the wind industry needs to almost triple its annual growth from 117 GW to 320 GW by 2030 (Global Wind Energy Council, 2024). With offshore wind farms bringing solutions to the climate change problem, it also brings challenges due to its environment particularities, being usually accompanied by high temperature, high humidity, typhoon, lightning, salt fog, among other issues (Kou*, et al.*, 2022). These conditions, in comparison to onshore wind farms, make offshore types provide higher failure frequencies, with blade adjustments, drivetrains and transmission systems being common failures (Cevasco; Koukoura; Kolios, 2021). The operational expenditure for offshore farms are also higher compared to onshore ones, provoked by longer downtime and more expensive transportation for maintenance teams (Asmussen; Liniger; Pedersen, 2021). A way to reduce operational costs could come from faster maintenance in conjunction with reliable fault detection systems.

Multiple surveys show that pitch systems are responsible for most failures, showing almost 13 % of all failures (Ribrant; Bertling, 2007), (Carroll; McDonald;

McMillan, 2016). Pitch systems can be categorized into two types: hydraulic and electro-mechanical types. Electric pitch systems have good accuracy and compactness, although limited torque capability (Yin*, et al.*, 2019). With hydraulic systems, torque capability increases, although precision is lower, as the relationship at higher pitch angle rates is non-linear (Zhang*, et al.*, 2013) and maintenance issues. Overall, electro-mechanical types are more common than hydraulic ones (Wei; Qian; Zareipour, 2020).

Pitch systems in wind turbines are key components for adjusting the angle of attack of the blades to optimize power output, as well as for stop protection in a cut-out speed (Jin*, et al.*, 2021). The harsh environment found in offshore farms usually brings large alternating loads, causing uneven distribution of forces throughout the pitch gearbox (Ha*, et al.*, 2021). Pitch systems can be constructed with different configurations, although one common component among systems are blade bearings with different compositions, as shown in Figure 10 (Jin*, et al.*, 2021). These components are found in either electro-mechanical and hydraulic types of pitch systems, with the latter not featuring gear teeth on the bearings (Liu; Zhang; Carrasco, 2020).

Figure 10 – Type of bearings found in pitch systems

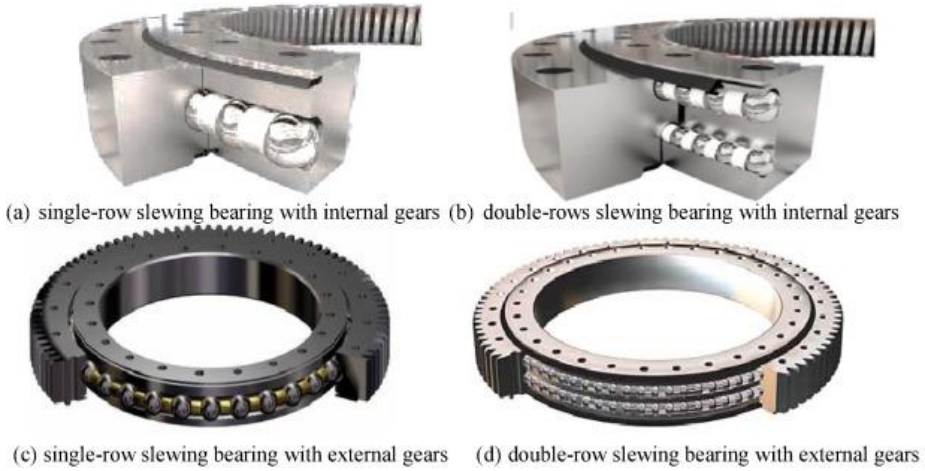

Source: Jin*, et al.* (2021).

Pitch systems manufacturers also experiment with different mechanism configurations in conjunction with bearings, being either passive or active pitch systems, based on the size of wind turbines (Wang*, et al.*, 2023). For smaller turbines, passive unified pitch systems are preferable as they do not need extra electric power

consumption for blade angle control (Chen; Shiah, 2016). Although, for bigger turbines, active systems are preferable for a better control of output power, even if manufacturing cost is higher (Zhang*, et al.*, 2025). Active pitch systems can be designed in various ways, as demonstrated by the Chinese manufacturer Pengky. One example, previously shown in Figure 7, features a worm drive integrated into the gear system, a configuration commonly used in small and medium-sized wind turbines, such as the one illustrated in Figure 11 A). For larger wind turbines, however, the mechanism shown in Figure 11 B) represents an independent electric pitch system that adjusts each blade individually, ensuring higher efficiency. Similarly, Figure 11 C) shows a comparable system but with a hydraulic-based mechanism.

Figure 11 – Different pitch mechanisms.

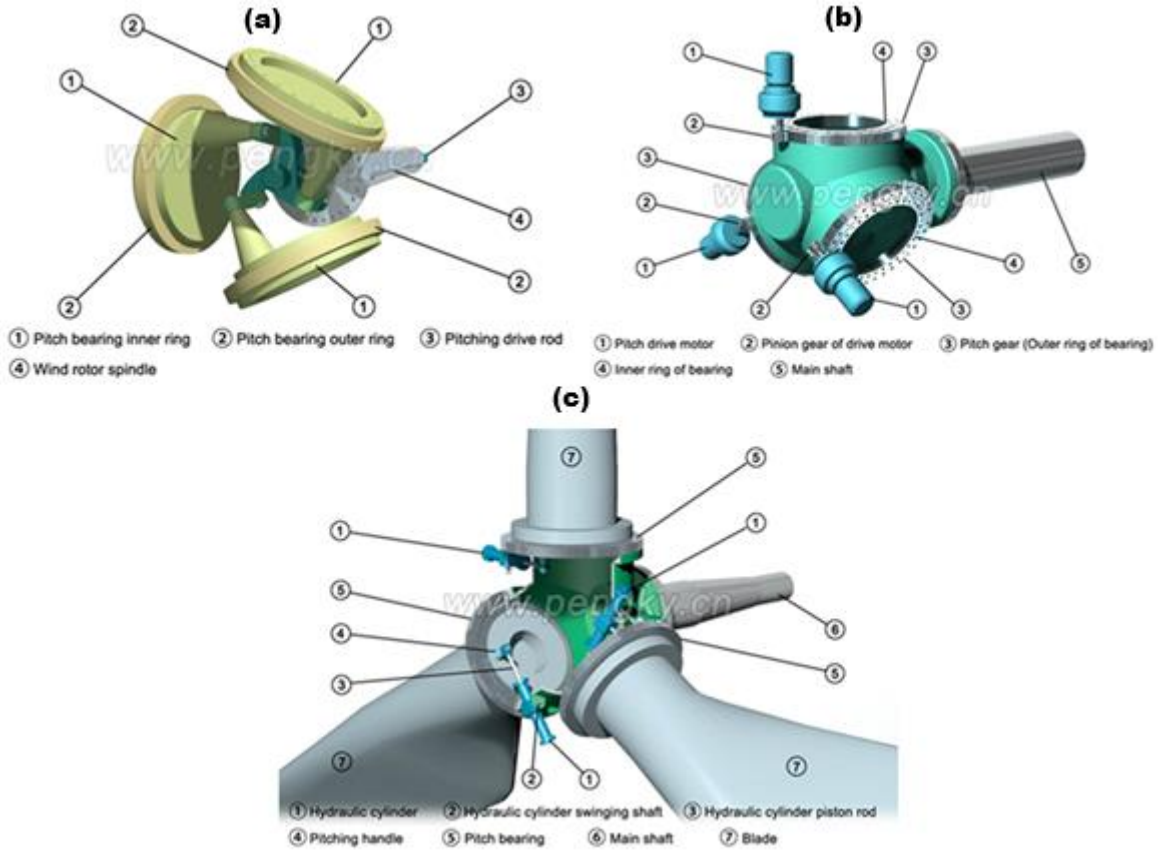

(a) Unified gear system (Pengky, 2019a), (b) Independent electric pitch system (Pengky, 2019c), (c) Hydraulic pitch system (Pengky, 2019c).

Worm drives are frequently used for power and motion transmission in industrial areas, as well as electric steering systems (Kim, 2018). It is used mostly for light gearboxes and can be used in high power needs (Chen*, et al.*, 2015). Common failures for these types of gears are surface fatigue, wear and tooth breakage

(Karabacak; Gürsel Özmen; Gümüşel, 2022). Worm drives also present multiple configurations, some with equidistant and non-equidistant threads, with different repair approaches for each type (Honkalas; Deshmukh; Pawar, 2021). DED based approaches for cladding have been conducted on worm wheels using bronze, as most gears it is the preferable material due to its ductility (Raghavendra*, et al.*, 2025). Although for worm drives, 42CrMo4 is the chosen steel material for its composition, due to its good machinability and high strength (Chaouch; Guessasma; Sadok, 2012).

2.2 Laser Additive Manufacturing

Laser-based remanufacturing technology offers effective solutions for repairing heavy-duty gears. It addresses key challenges such as controlling cracks in the clad layer, achieving high performance on the cladded tooth surface, and minimizing heat input (Shiyun Dong*, et al.*, 2008). Additionally, the process provides economic advantages through efficient material utilization, high welding speeds, automation, and reduced pre- and post-processing requirements (Nowotny*, et al.*, 2007). When cladding components with complex geometries, such as worm drives, powder-fed LMD is often preferred over wire-fed techniques, as it performs better in such applications (Raghavendra*, et al.*, 2025). Despite its advantages, powder-based deposition is generally less efficient than wire-based methods due to higher material consumption and the increased cost of powder feedstock (Ahn, 2021). In Figure 12, an illustration of the powder based LMD process on a cylindrical bar is shown.

Figure 12 - Schematic representation of an L-DED process on a cylindrical bar

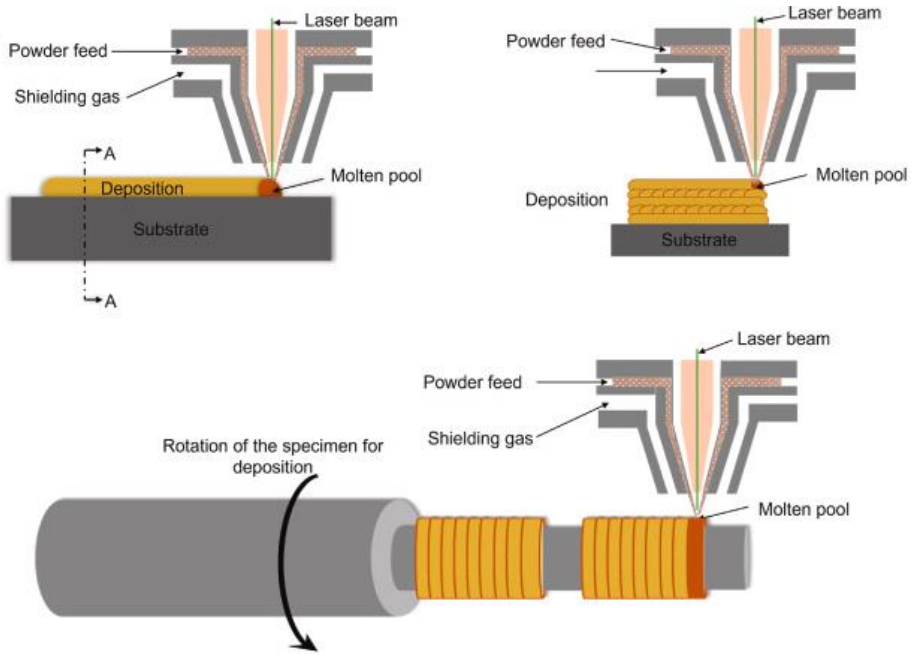

Source: Adapted from Raghavendra*, et al.* (2025).

Due to its characteristics, LMD presenting a low dilution rate results in superior surface properties compared to conventional treatment technologies. These include improved resistance to wear, corrosion, heat, and oxidation, as well as enhanced electrical properties, making it an attractive option for armoring applications (Cheng*, et al.*, 2022). LMD can remanufacture core components, extending the service life while reducing maintenance downtime and costs (Cheng*, et al.*, 2022). Additionally, the heat concentration of the laser allows for tooth and blade tip build-up with minimum distortion, and bearing, seal and drive surfaces, considered non-repairable by conventional welding techniques, can be effectively restored using LMD (D D Gu*, et al.*, 2012).

LMD strongly depends on the material and process characteristics and its attributed variables (D D Gu*, et al.*, 2012). For powder-based processes, variables such as flowability, chemical composition, particle shape, size, and distribution significantly influence the final product quality (Montero*, et al.*, 2016; Zhang*, et al.*, 2023). Additionally, process parameters such as laser spot size, laser type and power, scan speed, layer thickness, and dwell time also play a critical role in determining the outcome (Cooke*, et al.*, 2022; González-Barrio*, et al.*, 2022). Although LMD is a promising alternative to conventional methods, it faces challenges when applied to

multi-material structures. Intrinsic issues, such as mismatched thermal properties, the formation of brittle intermetallic phases, and varying laser absorptivity, can result in reduced material performance (Pellizzari*, et al.*, 2022). Additionally, LMD suffers from residual stress, which arise from the repeated cycles of rapid heating and cooling during the process (Ji*, et al.*, 2024).

2.3 Thermal Expansion

The 42CrMo4 1.7225 (AISI 4140) steel, a commonly used material for cladding, is renowned for its high strength, good machinability and robustness (Chaouch; Guessasma; Sadok, 2012). This low-alloy steel is used in multiple applications, including crankshafts, bolted assemblies, forged and welded components (Lin; Chen; Zhang, 2009), (Andreatta*, et al.*, 2023). As with any material, thermal expansion must be considered when analyzing their behavior in near-extreme temperatures. For that, stress-free dilatometry tests were performed on 42CrMo4 in a study by (Areitioaurtena*, et al.*, 2022). A heating rate of 20 °C/s was set to reach 900 °C on 4x10 mm cylinder specimens, with also different cooling rates used to reach multiple microstructural phases. Figure 13 illustrates the relative change in length and the coefficient of thermal expansion (CTE) as they vary with temperature. It is evident that variations in the microstructure due to temperature change have different length increments. This temperature and microstructure dependence that CTE has is also described in (Gulpak; Sölter, 2015), (Papuga*, et al.*, 2023), and (Neumann; Böhlke, 2016). Significant thermal expansion can lead to misalignment between the planned and actual deposition track.

Figure 13 - Relative change in length versus temperature [°C] on the left. CTE versus temperature [°C] on the right.

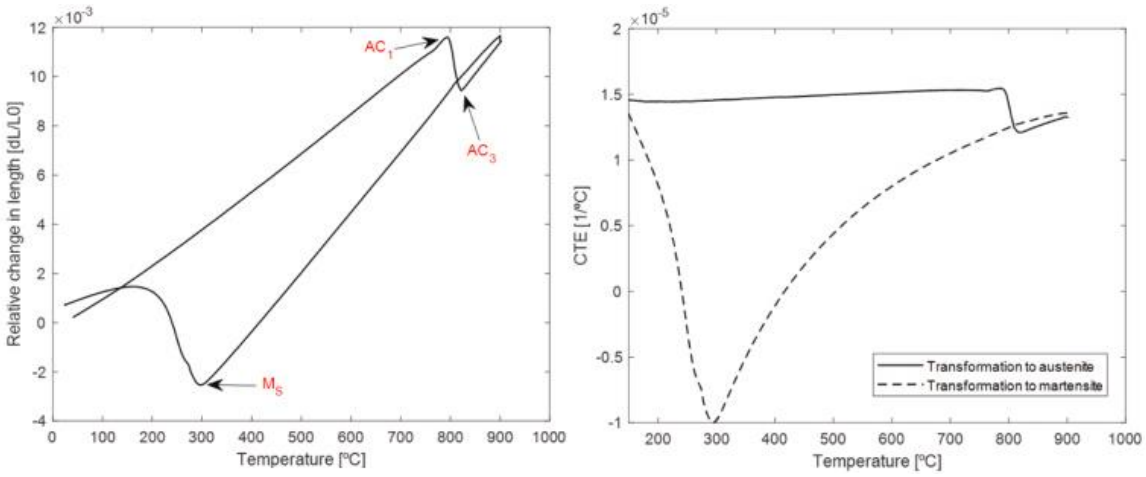

Source: Adapted from Areitioaurtena*, et al.* (2022).

In a study by (Behrens*, et al.*, 2017), thermal-mechanical behaviors of cylindrical 42CrMo4 specimens were examined with and without load. The specimens were heated to 950 °C for 5 minutes, then cooled down along a nearly exponential time-temperature trajectory. It was observed that there existed a linear longitudinal contraction due to cooling from 950 °C, as well as an elastic length change at 400 °C due to load onset. Without load, volume changes were only noticed below 310 °C, due to martensitic transformation. (Cooke*, et al.*, 2022) also conducted a thermal-mechanical study using 42CrMo4 steel, but with Laser-Direct Energy Deposition. Three cases of 20-layer thin walls, each measuring 37 x 3.6 x 6 mm, were deposited with varying dwell times between each layer depositions: 0s, 20s and 40s. It was observed that the microstructure was affected due to changing dwell times, leading to different CTE for the same material, as demonstrated in (Fernandez-Sanchez; Iza-Mendia; Jorge-Badiola, 2024). Thermal properties, including conductivity, melting point and CTE usually vary in different materials, leading to thermal-stress-induced defects such as cracks and pores (Pellizzari*, et al.*, 2022). Varying geometry due to thermal expansion may misalign the planned track with actual track position, leading to lower quality finished products.

2.4 Sensor-Aided Control

To enhance the automation capabilities of LMD and reduce errors, many studies have focused on developing advanced control systems. These systems follow different approaches: some are designed to monitor specific variables during the process (open-loop systems), while others actively adjust parameters in real time based on feedback data (closed-loop systems) (Montero*, et al.*, 2016).

LMD brings many parameters affecting the overall quality of the finished product. Some of the most commonly studied parameters are laser power, powder feeding rate, temperature, scanning speed, beam shape, surface roughness, shielding gas, melt pool morphology, thermal expansion, among others (Bernabe Carcel*, et al.*, 2010). In both industry and research, sensor configurations for LMD are widely employed, such as Proportional-Integral-Derivative (PID) controllers, in a closed-loop environment, based on melt pool size and temperature (Banfi*, et al.*, 2022), acoustic sensing (Kim; Park, 2024), or 3D scanning (Vandone*, et al.*, 2020). Two-color pyrometers are usually employed when temperature is the parameter of choice to control. The sensor is independent of the emissivity of the material, compared to one-color variants, as well as a contactless solution suitable for LMD applications (Bernabe Carcel*, et al.*, 2010). The implementation of track height control is also sometimes utilized by installing multiple off-axis sensors (Xin*, et al.*, 2020), although off-axis methods usually limit head freedom leading to collisions (Banfi*, et al.*, 2022). Although these sensors aid in controlling multiple variables, the geometry in itself can still vary (Garmendia*, et al.*, 2018; Vandone*, et al.*, 2020).

LMD characteristics such as heat accumulation, cooling rates, and varying thermal expansion can lead to unexpected effects on the fabricated part, including inadequate dimensional accuracy. Therefore, continuous monitoring and geometry control are essential to stabilize the process in industrial applications (Vandone*, et al.*, 2020). In Vandone*, et al.* (2020) authors employed a 3D scanner to capture the geometry of the partially manufactured part and compared it to the target geometry. Based on the discrepancies identified between the expected and actual geometries, a revised part program was generated and executed to correct deviations. Figure 14 shows the forming of the actual geometry with a point cloud-based scanning illustrated in a heat map.

Figure 14 – Built part (left) and heat map reconstructed (right)

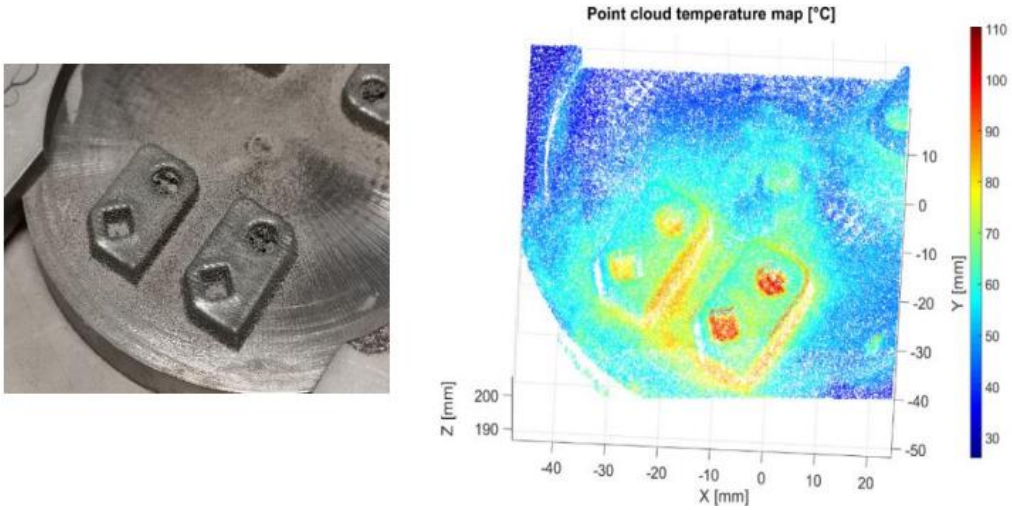

Source: Vandone*, et al.* (2020)

Results demonstrated that the system's geometric accuracy (< 0.03 mm) is sufficient for detecting deviations in LMD, where process uncertainties can cause dimensional variations of a similar magnitude within a single deposited layer. In Baraldo*, et al.* (2020) authors proposed a monitoring configuration based on beam-coaxial imaging controlling laser power with planned geometry as reference, improving the accuracy of deposited tracks with complex features. The closed-loop control showed good results, diminishing over-shootings by 17 %. The work done by Garmendia*, et al.* (2018) implemented a control strategy targeting both component geometry and material morphology, utilizing a laser line profiler in conjunction with a high-speed infrared camera. The strategy involved real-time control of standoff distance, deposition velocity, and laser power. Executed on a layer-by-layer basis, the control process was divided into two distinct phases: a measurement phase, which generated a deviation map from point cloud data, and a deposition phase, in which the computed deviations were used to dynamically adjust the process. Although the method effectively compensated for geometric deviations, it resulted in increased processing time.

In the present work, due to the way the chosen geometry consists of, point-cloud based data provided by a profiling scanner needs to be understood and classified. Consequently, techniques for reliably identifying features such as edges and valleys must be validated and thoroughly tested. In Ni*, et al.* (2016) it is described that 3D edge detection extracted from laser scanning data can be characterized into two

groups: direct methods, which first recognizes the points, clustering them into planes, detecting edges and extract feature lines and outliers; indirect methods, which first convert a 3D point cloud into an image, detecting 2D edges and projecting these 2D edges to obtain 3D edges.

Edge detection can be employed by checking if a random point is on a surface boundary, where there will be an angular gap between neighboring points. If the random chosen point is an interior point, the angle between neighboring points will be consecutive, with no substantial gap (Ni*, et al.*, 2016). This technique utilizes the Random Sample Consensus (RANSAC) algorithm, where it identifies the outliers in a data set estimating the desired model using outlier-free data (MathWorks, 2025). For a sharper edge detection, normal vector estimation from a 3D point-cloud is required (Dena Bazazian; Josep R. Casas; Javier Ruiz-Hidalgo, 2015). Normalization combined with neighboring angle checking is mentioned in multiple works, like in Wu*, et al.* (2024) and Li*, et al.* (2025). These strategies must be analyzed and employed in each dataset to verify its overall applicability.

3 MODELLING, TRIALS AND SIMULATIONS

This chapter presents the experimental setup and methodology used for high precision 2D profile scanning of a worm drive at the Fraunhofer Institute for Laser Technology (ILT) in Aachen, Germany. A series of linear scan trials at different speeds and surface conditions were performed, using C++ and python written software, to evaluate scan quality and the results were analyzed through 3D simulations based on collected X, Z, and inferred Y data.

3.1 Modelling

This study was carried out on a seven-axis Computer Numerical Control (CNC) machine manufactured by Karl H. Arnold Maschinenfabrik GmbH & Co. KG shown in Figure 15, outlining the sensor in yellow and the nozzle in blue. The setup includes a powder feeder from Oerlikon Metco AG, which delivers material via a hose using argon as the carrier gas. Additionally, a TRUDISK 5001 solid-state Nd:YAG diode laser from TRUMPF GmbH is connected to the laser head through a fiber optic cable. This laser can reach a maximum power output of 5 kW and operates at a wavelength of 1030 nm.

Figure 15 – Seven-axis CNC machine

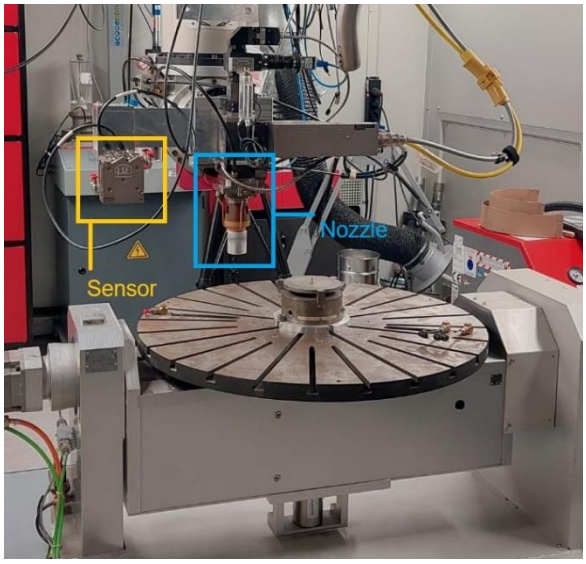

Source: Own (2025) and Fraunhofer ILT (2025)

The seven axes of the CNC machine, illustrated in Figure 15, can be found in a profile schematic shown in Figure 16. Two axes, C2 and A2 are responsible for the rotation and tilt angle of the table, respectively. The other five axes oversee the head movement.

Figure 16 – Machine axis profile schematic

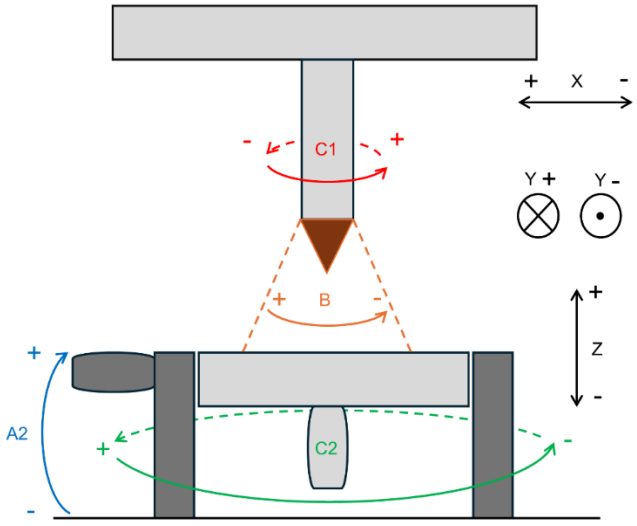

Source: Own (2025) and Fraunhofer ILT (2025).

For this work, almost all the axes shown in Figure 16 are used, with the only exception being the B axis, which controls the tilt angle of the head. Among the various sensors integrated into the machine, the focus of this work is on the high-speed laser profile scanner *scanCONTROL 2950-100 /BL* developed by Micro-Epsilon, a leading manufacturer of precision sensor technology (Micro-Epsilon, 2025b). This sensor features a 100 mm measurement range and utilizes a blue laser line with a wavelength of 405 nm. The blue laser was chosen for its superior precision and its ability to accurately measure surfaces of red-hot glowing materials, where conventional red lasers would be less effective. The laser scanner utilizes the laser triangulation principle for two-dimensional profile detection (Micro-Epsilon, 2025b), shown in Figure 17.

Figure 17 – Measuring principle of laser scanners

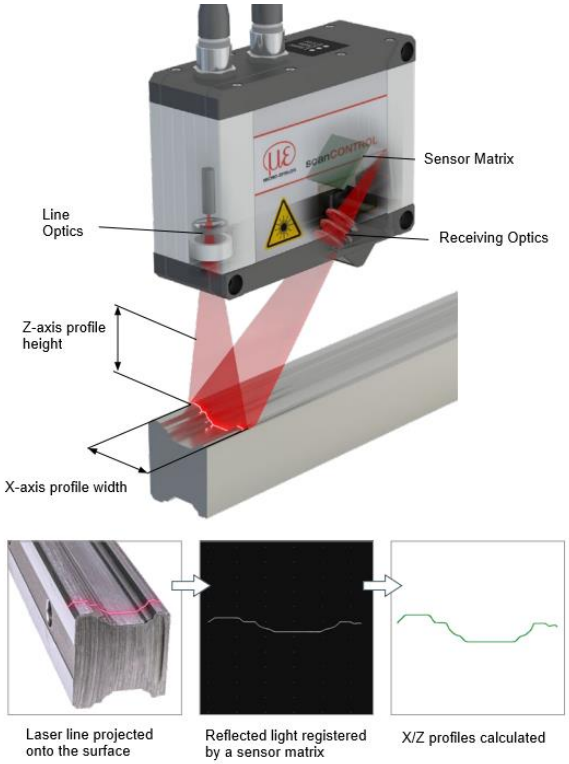

Source: Adapted from Micro-Epsilon (2025b)

The laser scanner captures only the 2D surface profile directly above the scanned area, as illustrated in Figure 17. Each profile consists of height (Z-axis) and width (X-axis) coordinates, calculated from individual pixels detected by the sensor matrix. For this sensor, the set resolution is 1280 × 1280 pixels, resulting in 1281 X and Z data points per scanned profile. Due to its reflection-based scanning method, parameters such as exposure time, profile time, and signal saturation play a crucial role in enhancing the quality of the captured profiles. The exposure time [µs] refers to the duration the sensor is exposed to reflected light through the shutter. The profile time [Hz], which depends on the exposure time, defines the frequency at which profiles are acquired. Saturation [%] indicates the signal intensity and is influenced by both exposure and profile time. According to the sensor manufacturer, optimal saturation should fall within the range of 70 % to 90 % (Micro-Epsilon, 2025b). As each scanned subject has different surfaces and levels of shininess, it is important to test different exposure and profile times to assure good saturation.

The subject of this work has particularities when being scanned by the environment shown, as the subject is a worm drive and has a considerable length of over 300 mm. Figure 18 shows the subject mentioned.

Figure 18 – Worm drive

Source: Own (2025) and Fraunhofer ILT (2025).

Due to the noticeable reflection of the untreated work subject shown in Figure 18, techniques to reduce its shininess were employed on the same drive with intent to diminish outliers caught by the sensor. The first technique was to apply an anti-reflection spray made for laser scanning to the subject, as Figure 19 shows.

Figure 19 – Worm drive coated with spray

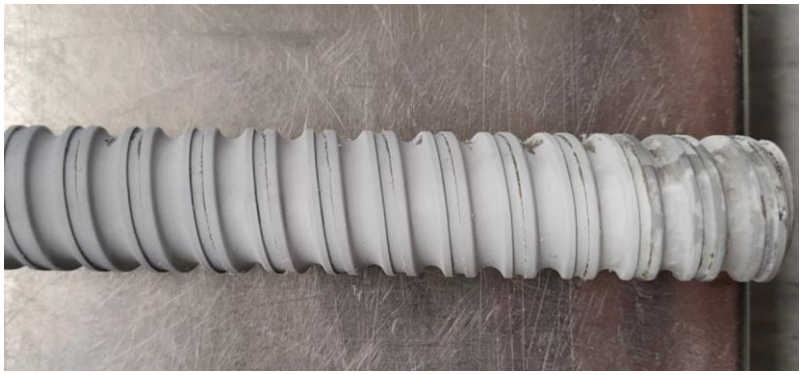

Source: Own (2025) and Fraunhofer ILT (2025).

The anti-reflection spray visibly diminishes the shininess, as shown in Figure 19. However, this method is not recommended during the deposition process, as the spray may interfere with the material behavior and affect the process outcome. For that, a second technique called sandblasting was employed. Sandblast uses compressed air to blast abrasive material against a surface. Figure 20 shows the outcome of this process.

Figure 20 – Worm drive coated with sandblasting

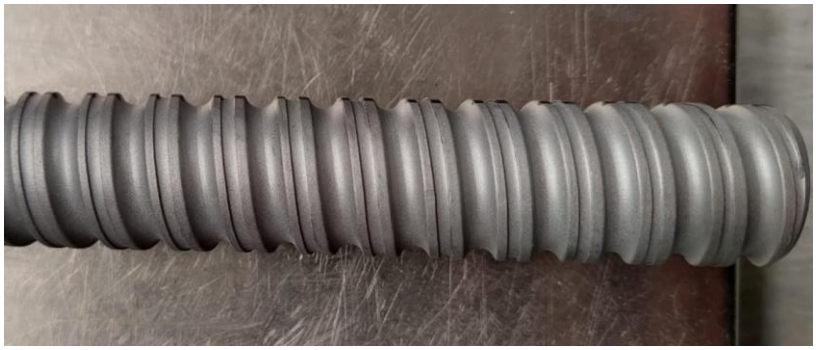

Source: Own (2025) and Fraunhofer ILT (2025).

It is visible in Figure 20 this method also achieves the desired effect and results in a more uniform appearance compared to the spray solution. However, it alters the original surface of the subject, making it rougher, a change that may be undesirable for certain applications.

3.2 Implementation

With the subject surface and sensor characteristics understood, a way to manipulate the captured data had to be developed. To communicate and extract that data from the sensor, Micro-Epsilon provides a Software Development Kit Version 4.1.1 (SDK) on their website (Micro-Epsilon, 2025a). The SDK enables integration of the sensor with custom applications developed in C++. With that in mind, a self-made C++ software was developed with the mail goal to record 2D (X and Z coordinates) profile data captured by the sensor and save each new profile in a Comma Separated Value (CSV) file format for further manipulation and simulation. This language was chosen not only due to its compatibility with the SDK, but also for its performance and reliability. Unlike interpreted languages such as Python, which are limited by interpreter locks, such as the Global Interpreter Lock (GIL), C++ offers significantly higher execution speed and more efficient resource management (Python, 2025). The flowchart of the software developed can be seen in Figure 21.

Figure 21 – Flowchart of the profile gatherer written in C++

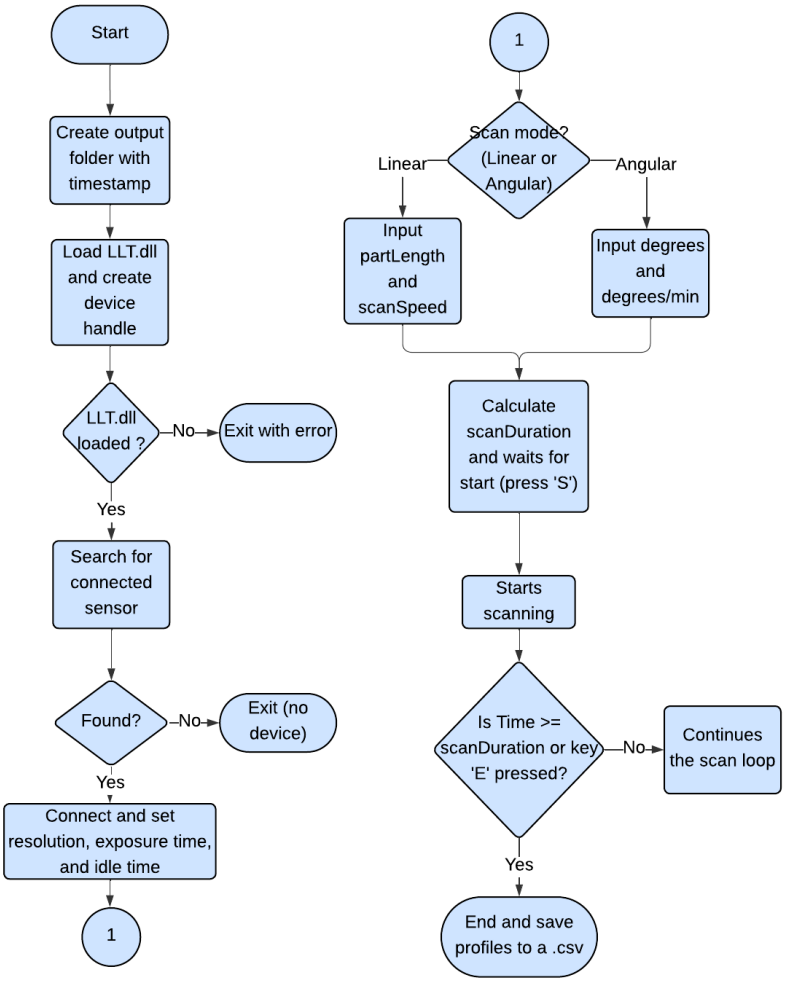

Source: Own (2025) and Fraunhofer ILT (2025).

The flowchart presented in Figure 21 can help one understand the scope of the software, which handles all stages of operation: from device connection and configuration to real-time data acquisition and storage. It starts by creating a unique folder using current date and time to store data from each session separately. The program attempts to load the Dynamic Link Library (DLL) provided by the SDK, to use the library functions. If no devices are found, or if the sensor was already connected to something else, the program displays an error message and closes. Once the program finds a device, it connects to it, retrieves the device name, and configures parameters such as resolution, exposure time, and idle time. The SDK does not let the user set profile time directly, and it configurates it using Equation 5 (Micro-Epsilon, 2025a).

$$Profile\ Frequency\ [Hz] = \frac{1}{(ExposureTime + IdleTime) \cdot 10\mu s} \quad (5)$$

After the program calculates the profile frequency, it asks the user to choose the scanning mode. In linear mode, the user provides the part's length and scanning speed given by the CNC machine. In angular mode, the user inputs the number of degrees wanted and rotation speed given, once again, by the CNC machine. This solution was implemented to synchronize the endpoint of the scan with the machine head's movement, as the two systems are not directly connected, and the software currently cannot access the machine's coordinate data. Before starting data acquisition, the program waits for the user to press the 'S' key on the keyboard. Once pressed, it enables profile transfer and enters a recording loop, depending on the profile frequency. During this loop, it checks whether the scan duration has been exceeded or if the user has pressed the 'E' key to promptly end it. Figure 22 shows the program prompt during the loop.

Figure 22 – Program prompt

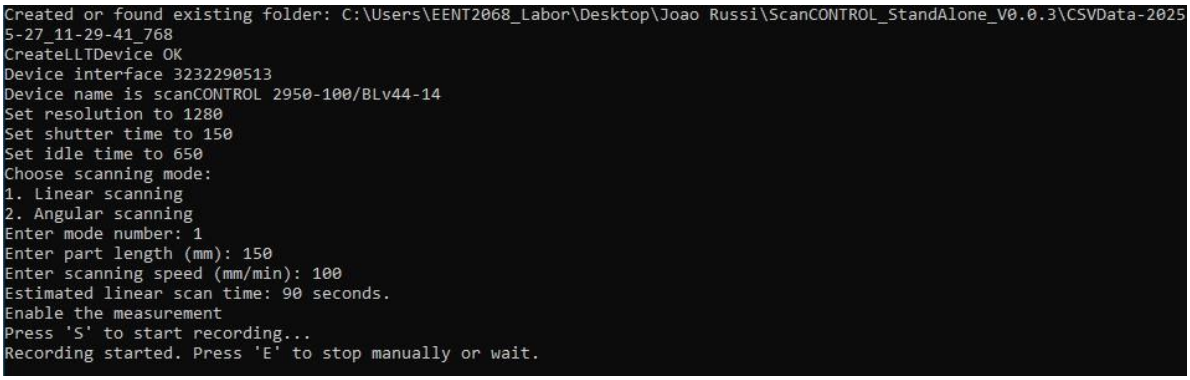

Source: Own (2025) and Fraunhofer ILT (2025).

For each profile captured, 1281 X and Z values are extracted, generating a timestamped filename, and saving the data to a CSV file inside the created output folder shown in Figure 22. After the loop ends, the scanner is disabled, lost profiles are reported, and resources are released properly.

3.3 Trials and simulation

When using the software to acquire profile data, the parameters must ensure a saturation level between 70 % and 90 %, as previously discussed. To achieve this, trial-and-error adjustments were made between profile frequency and exposure time using the manufacturer's profile viewer. Optimal saturation was reached with an

exposure time of 1.5 ms and a profile frequency of 125 Hz. According to Equation 5, this requires an idle time of 6.5 ms. A linear scan was then performed on the test samples to evaluate scan quality for different surface conditions: first on the raw subject, followed by the sprayed, and finally the sandblasted surface. Each sample was scanned twice at different speeds: 50 mm/min and 100 mm/min, to assess whether slower scanning reduces the number and frequency of outliers, totaling 6 trials. The subject was then fixed on the table using a clamp as Figure 23 shows.

Figure 23 – Subject fixed on the table

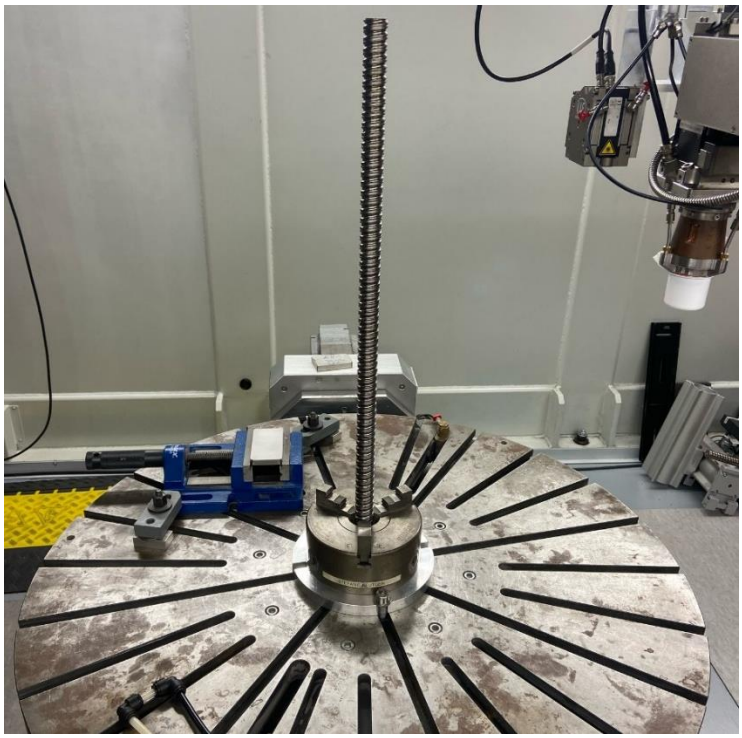

Source: Own (2025) and Fraunhofer ILT (2025).

As can be seen in Figure 23, the scanner will not see the subject using this position. For that reason, both the A2-axis and C1-axis of the CNC machine rotated 90°, leading to a position depicted in Figure 24.

Figure 24 – Work position with A2 and C1 both tilted 90°

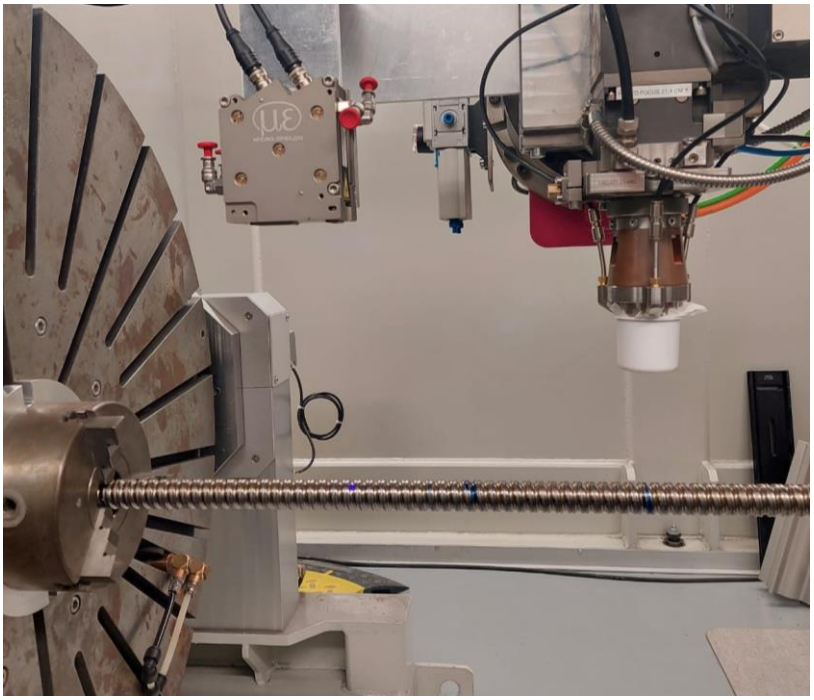

Source: Own (2025) and Fraunhofer ILT (2025).

As Figure 24 illustrates, the scanner moves in the negative direction of Y. Therefore, the program must halt the scanning process before the machine head collides with the inclined table, with 170 mm being the length chosen for all trials. Due to the three dimensionality of the scan, the Y-axis was reconstructed treating each CSV file as a “slice” along the axis (length of a part or angular progression). But because the files themselves contain only X and Z coordinates, the Y-coordinate must be inferred based on the file index and total scan length. For each trial, simulations using 3D plots created with python are presented as heat maps based on Z-values, visualized from three different angles. In these maps, darker colors represent lower Z-values, while lighter colors indicate higher elevations.

3.3.1 Trial 1

The first trial utilized the raw subject employing a scanning speed of 50 mm/min. **Error! Not a valid bookmark self-reference.** shows the fetched X and Z coordinates, as well as the simulated Y-axis.

Figure 25 – Raw subject with scanning speed of 50 mm/min. (a) View from above. (b) View from the side. (c) Isometric view.

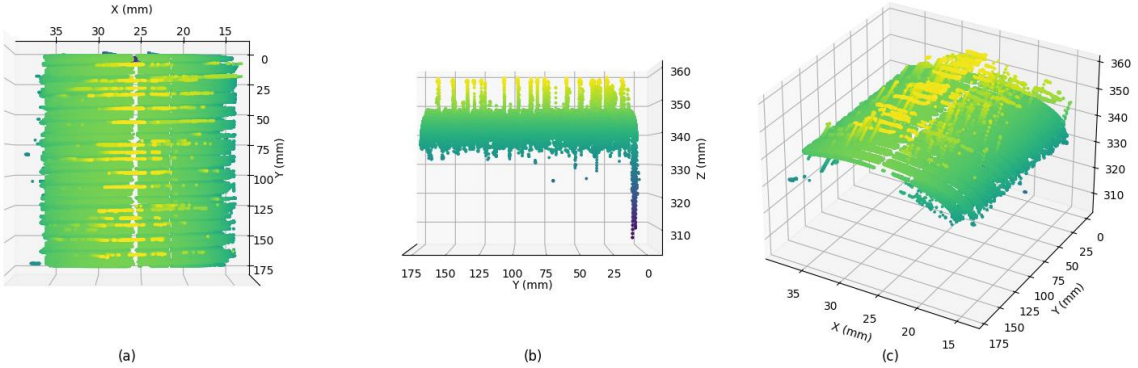

Source: Own (2025) and Fraunhofer ILT (2025).

As shows Figure 25, multiple outliers are present, likely caused by the surface shininess of the untreated subject. The high number of outliers compromises data quality, highlighting the need for robust and intelligent data processing methods. In Figure 26 the outliers are shown using the orange color.

Figure 26 – Outliers on the raw subject with scanning speed of 50 mm/min. (a) View from above. (b) View from the side. (c) Isometric view.

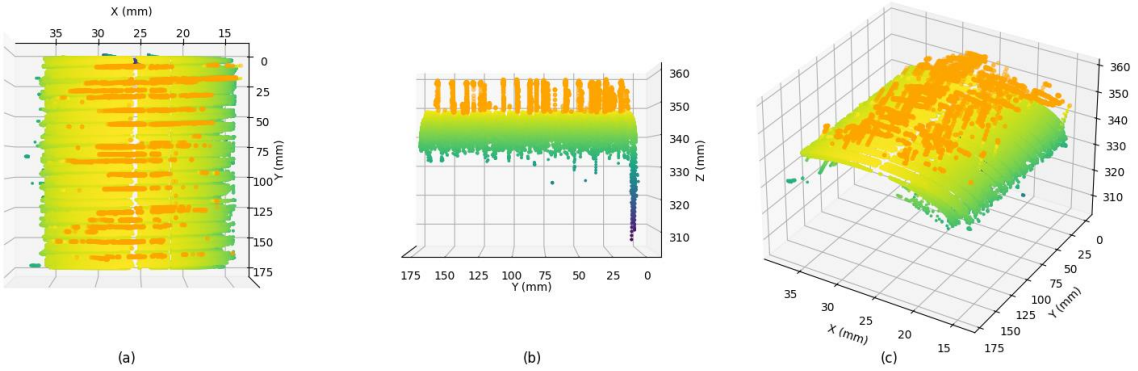

Source: Own (2025) and Fraunhofer ILT (2025).

Analyzing only the positive Z outliers, those that visually compromise edge detection in Figure 26, reveal a total of 5646 such points, representing 1,05% of all scanned values.

3.3.2 Trial 2

The second trial utilized the raw subject employing a scanning speed of 100 mm/min. Figure 27 shows the fetched X and Z coordinates, as well as the simulated Y-axis.

Figure 27 - Raw subject with scanning speed of 100 mm/min. (a) View from above. (b) View from the side. (c) Isometric view.

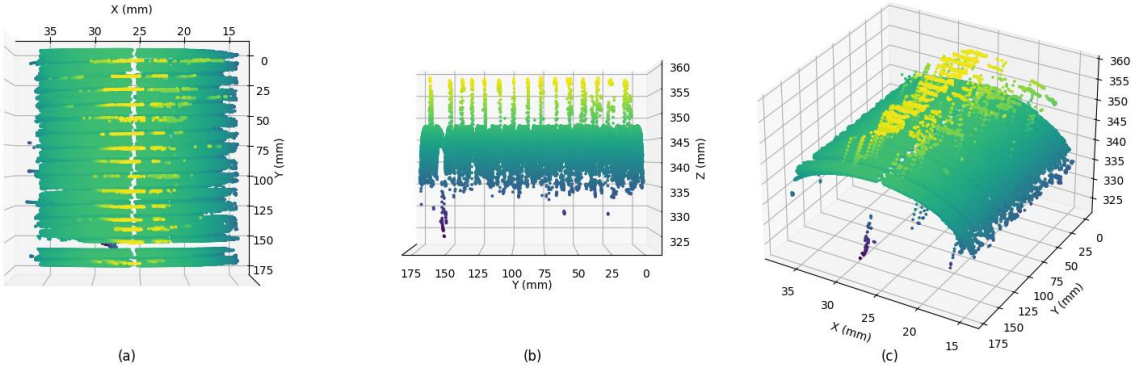

Source: Own (2025) and Fraunhofer ILT (2025).

As shown again in Figure 27, multiple outliers are present on the raw sample, likely due to surface shininess, with even a visible gap in the plot. In Figure 28 the outliers of the raw subject with 100 mm/min scanning speed are shown in the orange color.

Figure 28 - Outliers on the raw subject with scanning speed of 100 mm/min. (a) View from above. (b) View from the side. (c) Isometric view.

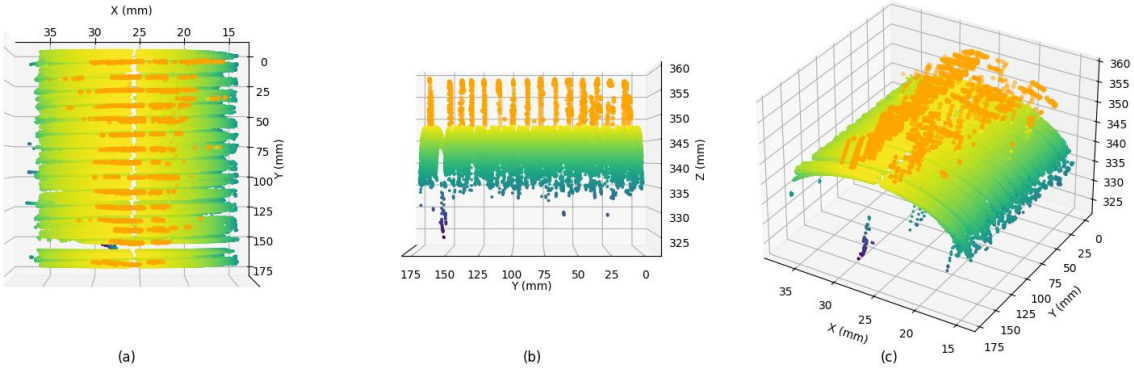

Source: Own (2025) and Fraunhofer ILT (2025).

Analyzing only the positive Z outliers, those that visually compromise edge detection in Figure 28, reveal a total 2529 of such points, representing 1% of all

scanned values. When comparing both trials, the percentage of outliers remains similar, with a slight reduction even at higher scanning speeds. However, the faster scan results in lower quality, evidenced by a visible gap.

3.3.3 Trial 3

The third trial now uses a pre-treated subject using anti-reflection spray employing a scanning speed of 50 mm/min. Figure 29 shows the fetched X and Z coordinates, as well as the simulated Y-axis.

Figure 29 – Sprayed subject with scanning speed of 50 mm/min. (a) View from above. (b) View from the side. (c) Isometric view.

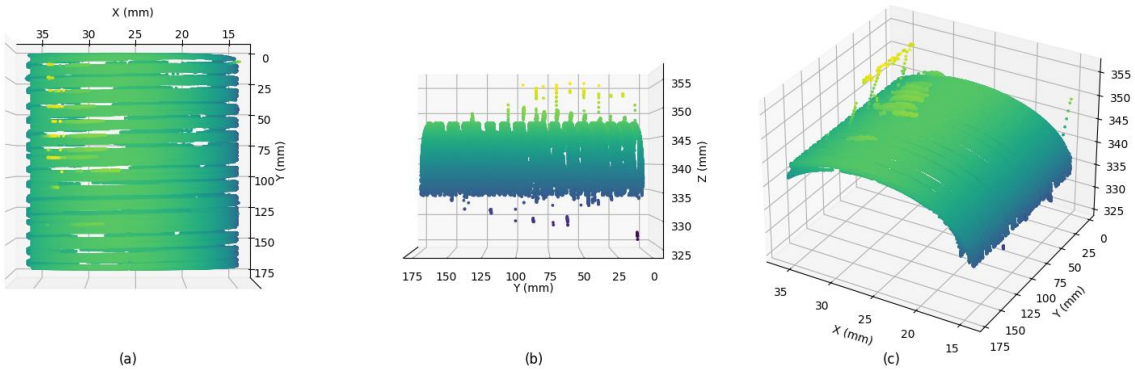

Source: Own (2025) and Fraunhofer ILT (2025).

As shown in Figure 29, fewer outliers are present on the sprayed sample compared to the raw one, likely due to surface shininess, with some visible gaps in the plot. In Figure 30 the outliers of the sprayed subject with 50 mm/min scanning speed are shown in the orange color.

Figure 30 - Outliers on the sprayed subject with scanning speed of 50 mm/min. (a) View from above. (b) View from the side. (c) Isometric view.

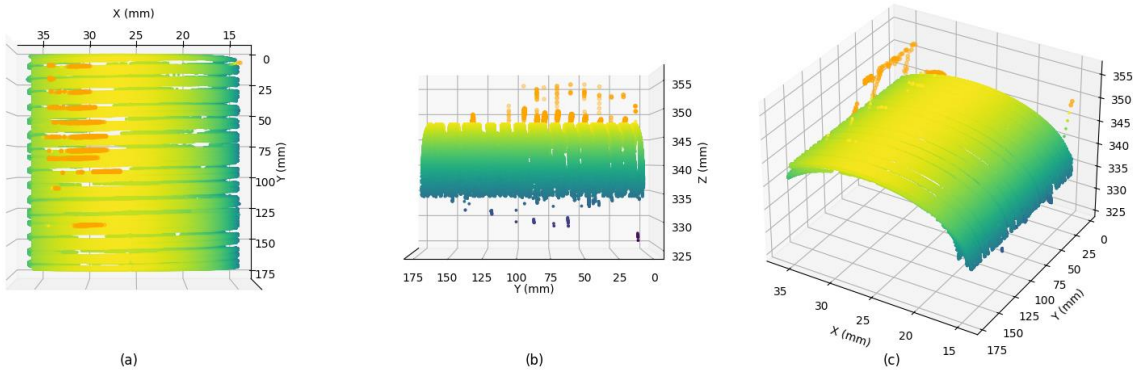

Source: Own (2025) and Fraunhofer ILT (2025).

Analyzing only the positive Z outliers in Figure 30, reveal a total of 1847 of such points, representing 0,33% of all scanned values. The number of outliers diminished when compared to the raw sample scans, and the overall quality of the scan is visually better.

3.3.4 Trial 4

The fourth trial now uses a pre-treated subject using anti-reflection spray employing a scanning speed of 100 mm/min. Figure 31 shows the fetched X and Z coordinates, as well as the simulated Y-axis.

Figure 31 - Sprayed subject with scanning speed of 100 mm/min. (a) View from above. (b) View from the side. (c) Isometric view.

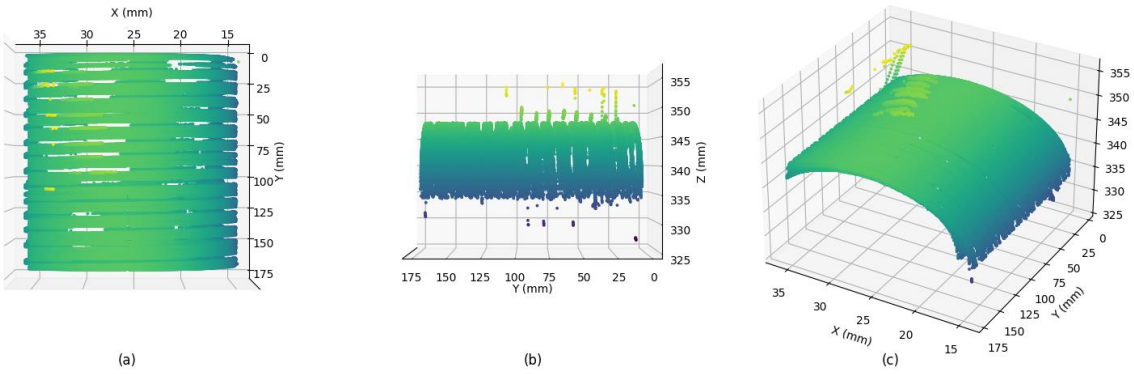

Source: Own (2025) and Fraunhofer ILT (2025).

As shown in Figure 31, a similar number of visible outliers are present on the 100 mm/min sprayed sample compared to the 50 mm/min one. Once again, in Figure 32 the outliers of the sprayed subject with 100 mm/min scanning speed are shown in the orange color.

Figure 32 - Outliers on the sprayed subject with scanning speed of 50 mm/min. (a) View from above. (b) View from the side. (c) Isometric view.

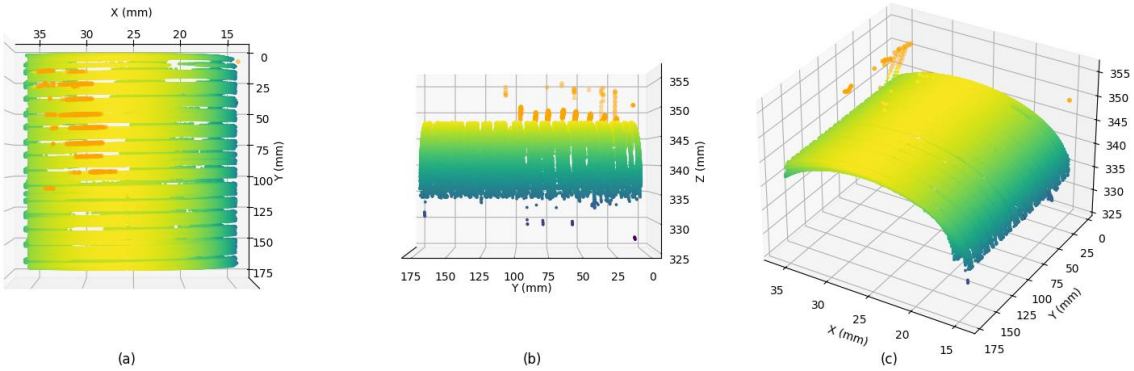

Source: Own (2025) and Fraunhofer ILT (2025).

Analyzing only the positive Z outliers in Figure 32, reveal a total of 869 of such points, representing 0.35% of all scanned values. The number of outliers diminished when compared to the raw sample and slower sprayed scans, although very similar.

3.3.5 Trial 5

The fifth trial now uses a pre-treated subject using sandblast employing a scanning speed of 50 mm/min. Figure 33 shows the fetched X and Z coordinates, as well as the simulated Y-axis.

Figure 33 - Sandblasted subject with scanning speed of 50 mm/min. (a) View from above. (b) View from the side. (c) Isometric view.

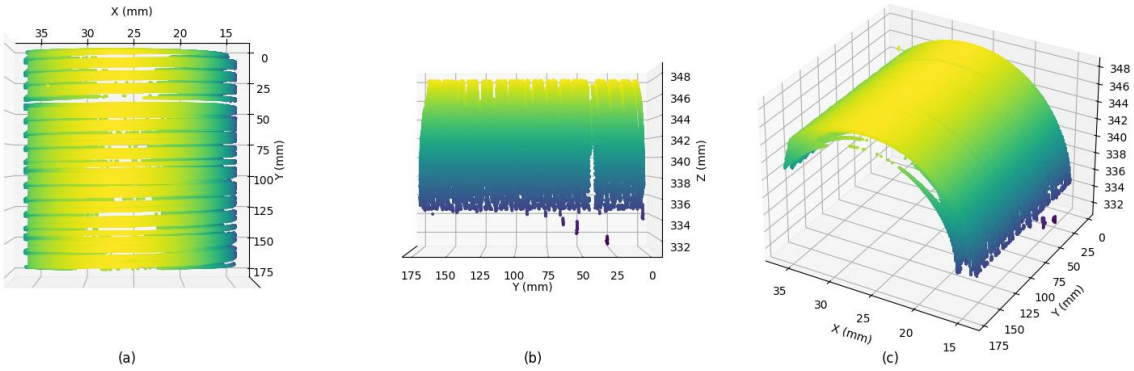

Source: Own (2025) and Fraunhofer ILT (2025).

As can be seen in Figure 33 , no apparent outliers are visible in the plot, with only a gap is present. Data analysis confirms that no Z-axis surface outliers were detected, indicating a significantly improved scan quality compared to both the raw and sprayed samples.

3.3.6 Trial 6

The sixth and final trial uses a pre-treated subject using sandblast with a speed of 100 mm/min. shows the fetched X and Z coordinates, as well as the simulated Y-axis.

Figure 34 - Sandblasted subject with scanning speed of 100 mm/min. (a) View from above. (b) View from the side. (c) Isometric view.

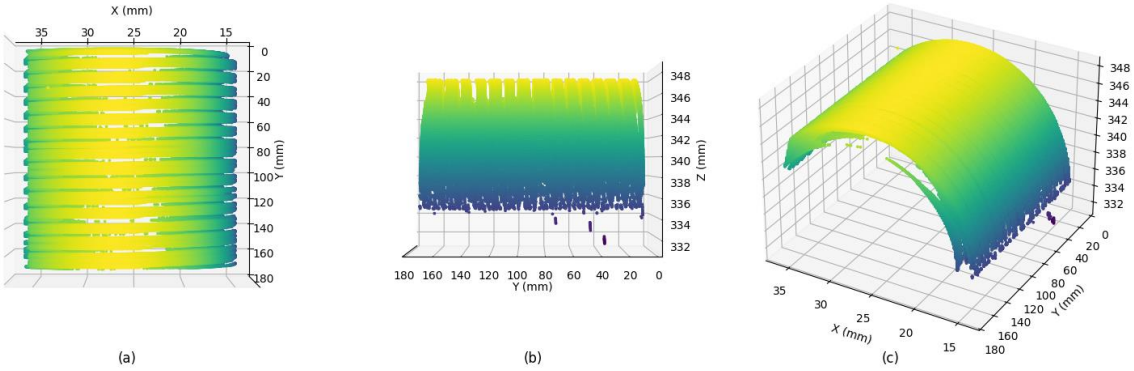

Source: Own (2025) and Fraunhofer ILT (2025).

As can be seen in Figure 34, once again, no apparent outliers are visible in the plot, with no gaps this time. Data analysis confirms that no Z-axis surface outliers were detected, indicating a significantly improved scan quality compared to both the raw and sprayed samples and even the slower sandblasted scan.

3.4 Considerations

The trials demonstrated that untreated surfaces, such as the raw worm drive, resulted in a considerable number of positive Z-axis outliers due to excessive reflection, undermining the quality and reliability of the captured profiles. Figure 35 shows a visual comparison between each surface with a 50mm/min scanning speed.

Figure 35 - Comparison between raw, spray and sandblast surfaces with 50 mm/min scanning speed

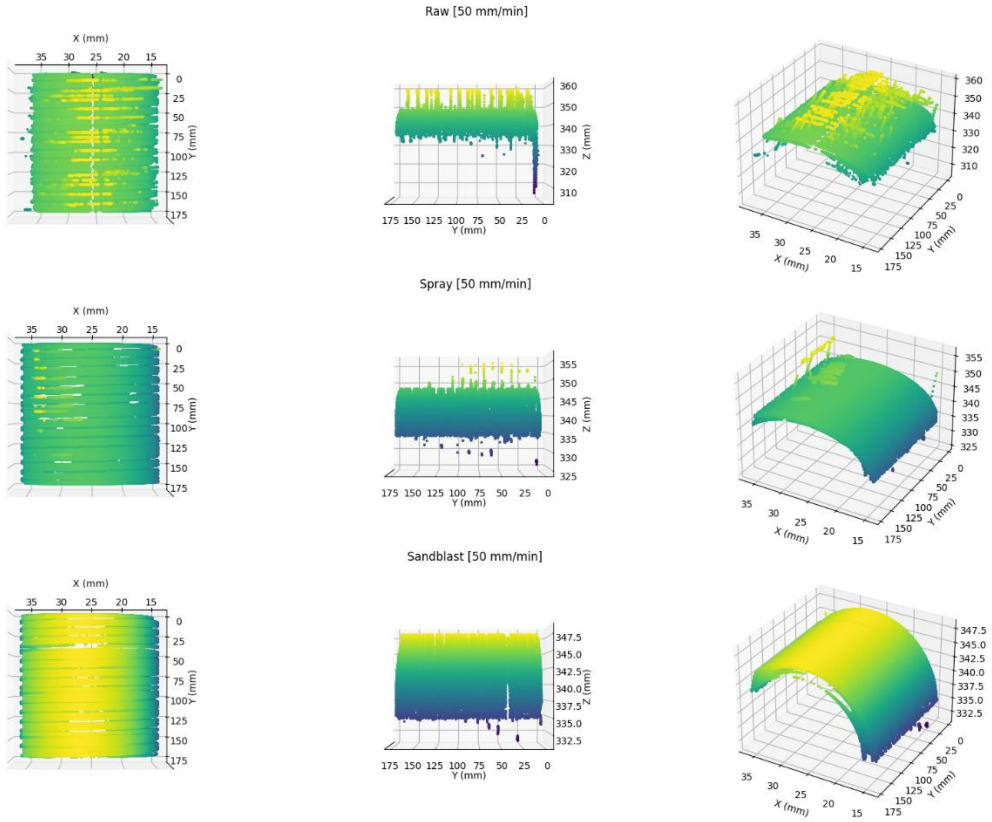

Source: Own (2025) and Fraunhofer ILT (2025).

As can be observed in Figure 35, the sandblasted surface shows a smaller number of outliers in the Z-axis, visually proving its superiority in this regard for a 50 mm/min scanning speed. Figure 36 shows the same visual comparison but for a 100 mm/min speed.

Figure 36 – Comparison between raw, spray and sandblast surfaces with 100 mm/min scanning speed

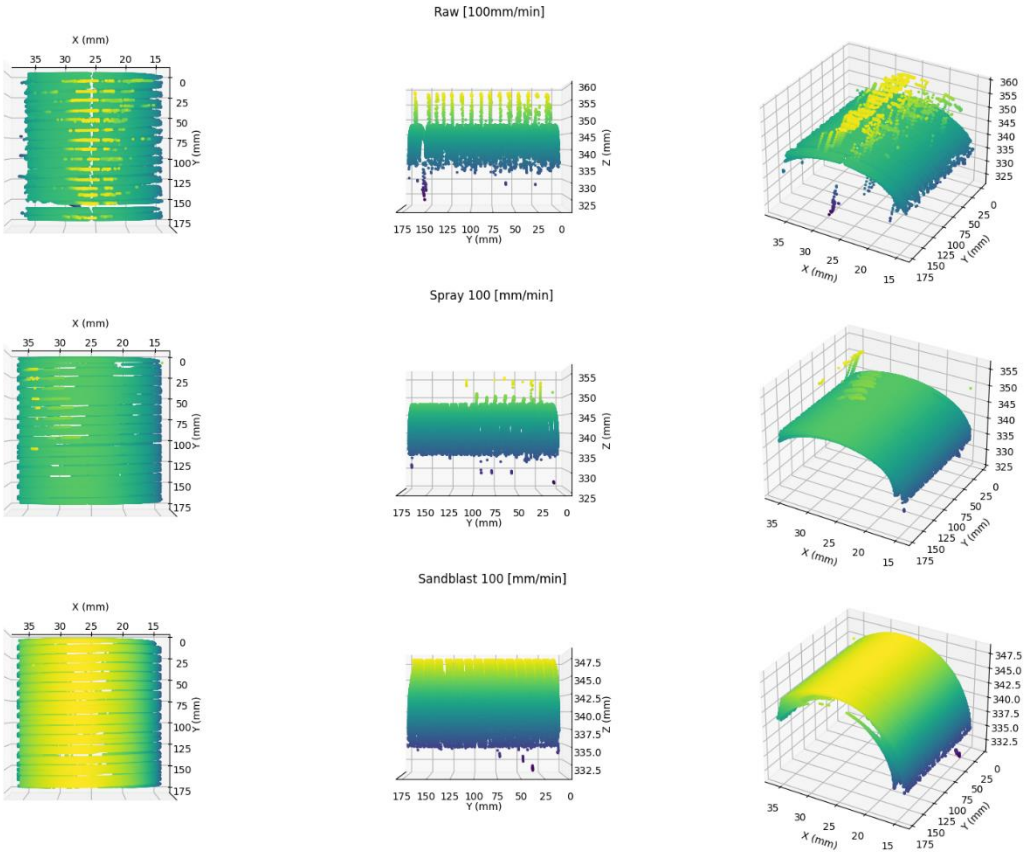

Source: Own (2025) and Fraunhofer ILT (2025).

In Figure 36 it can be also seen that sandblast visually shows less outliers in the Z-axis, proving it better than the other two surfaces also in the 100 mm/min speed. Although while in both cases the sandblasted surface shows better results, this needs to also be evaluated using a numerical approach. For that, a scale gain strategy, shown in Table 1, was applied to determine the optimal scanning speed and surface. This strategy assumes that if the scanning speed doubles, the number of outliers should also double, assuming a linear relationship. If this is not the case, for example, if the number of outliers decreases or increases by less than double, then the higher speed results in more scans per minute with fewer or comparable outliers, making it the preferred option. Conversely, if doubling the speed leads to a proportional or greater increase in outliers, the slower scanning speed becomes the better choice, despite the longer scanning time.

Table 1 – Outlier comparison between speed and surfaces by the scale gain approach

Outliers in Z					
Surface	**Speed [mm/min]**	**Number of valid points**	**Number of outliers**	**Ratio of outliers**	**Scale Gain**
Raw	50	563968	5646	1,00%	-
	100	267071	2529	0,95%	45%
Spray	50	555307	1847	0,33%	-
	100	245541	869	0,35%	47%
Sandblast	50	621135	0	0	-
	100	278042	0	0	0

Source: Own (2025) and Fraunhofer ILT (2025).

Table 1 shows that the number of outliers decreases by nearly half, 45% for raw surfaces and 47% for sprayed surfaces, when the scanning speed is doubled from 50 mm/min to 100 mm/min. This supports the visual analysis of the scan data, indicating that both sandblasted surfaces and higher scanning speeds result in cleaner, quicker, and more reliable scans. Consequently, the 100 mm/min sandblasted scans were selected as the reference for the edge detection methods discussed in Chapter 4.

4 RESULTS

To tackle geometric distortions caused by thermal expansion during laser-based deposition process, a way to correct planned track position with actual track position must be developed. For that, this chapter presents and evaluates possible edge detection approaches. Misalignment between programmed and actual track positions can compromise build quality, as shown in Chapter 2, making it essential to reliably distinguish edge regions from crevices in the point cloud data. Each approach was applied to real scanning data, and their effectiveness in minimizing false edge detections while maintaining reasonable processing times is discussed, ultimately guiding the selection of the most suitable strategy for integration into future correction systems.

4.1 Edge detection approaches

As previously mentioned in chapter 2, thermal expansion can cause misalignment between the programmed and actual track positions, potentially compromising the final geometry and needing correction. To better organize the data, identify patterns, and eventually provide input to a control system, it is essential to categorize regions as either edges or crevices, where 'edges' refer to the gear threads intended for deposition tracks. To achieve this, in this work three different edge detection approaches were developed to enable accurate categorization of the scanned surface regions.

4.1.1 First approach – Difference between neighbors

The first approach calculates the difference between consecutive Z values along the scan profile using Equation 6.

$$\Delta Z_i = Z_{i+1} - Z_i \;\; \forall \;\; i = \; 0,1, \dots, N-2 \tag{6}$$

By analyzing the frequency of these differences created using Equation 6, the most common ΔZ can be identified. The optimal ΔZ value is selected based on which one results in the fewest crevice points being falsely detected as edges. To

visualize the most common gaps between neighboring 3D points, the 10 most common ΔZ values are highlighted in red and other values are in grey. This can be seen in Figure 37.

Figure 37 – 10 most common ΔZ values using sandblast 100 mm/min data

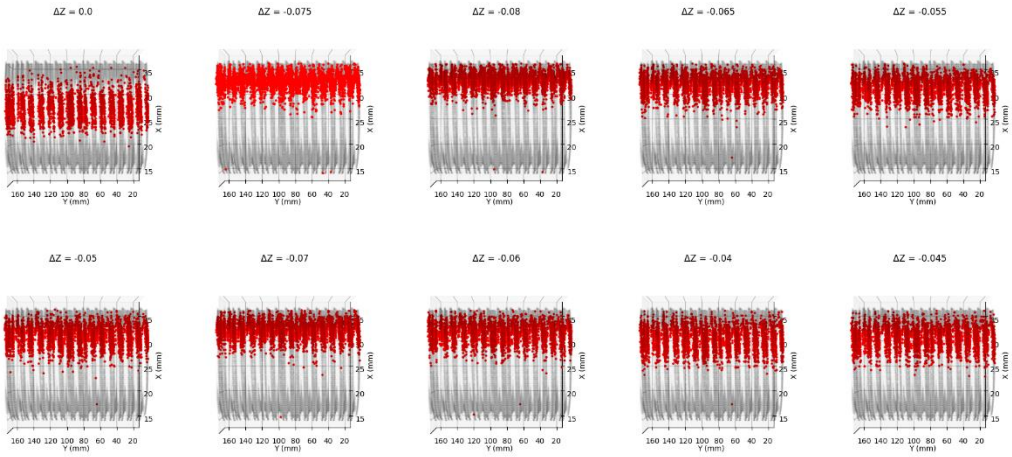

Source: Own (2025) and Fraunhofer ILT (2025).

It can be observed in Figure 37 that most ΔZ values detect edges but also crevices, with values such as 0,0 and -0,04 showing smaller amounts of highlighted crevice points. Figure 38 shows only ΔZ = 0,0 points highlighted with different observation angles.

Figure 38 - ΔZ = 0,0 highlighted of the sandblasted subject with scanning speed of 100 mm/min. (a) View from above. (b) View from the side. (c) Isometric view.

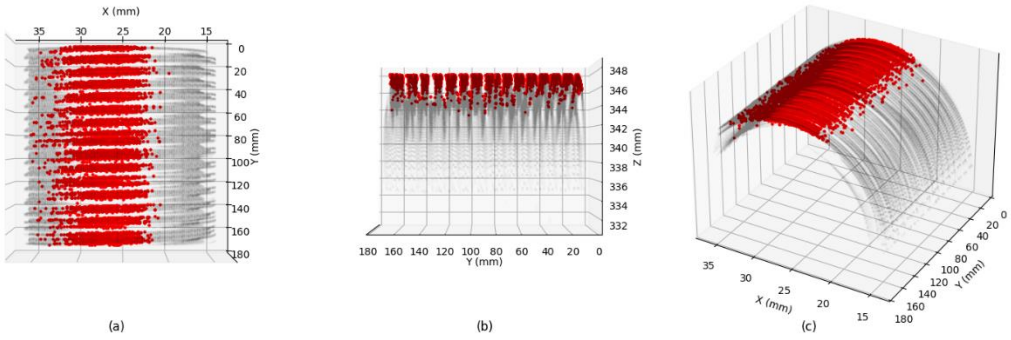

Source: Own (2025) and Fraunhofer ILT (2025).

In Figure 38, although this approach successfully identifies a significant number of edge points, it also incorrectly classifies some crevice points as edges, even when picking one of the visually better ΔZ. Also, this approach showed to be very quick when simulating and with low computing power, needing only 3,1 seconds for it.

4.1.2 Second approach – Neighboring Angles

The second approach first normalizes the data points to [0,1] creating a normal vector for each point, then the script builds a K-dimensional tree for neighboring search, comparing surface normals of each point to its neighbors, looking for pairs whose angle between normals is close to 0°, calculated by Equation 7. A normal vector is a vector that is perpendicular to a surface at a given point, if it is on a flat wall, all normals point in the same direction. If one point is found within the threshold, the point is the flagged as an edge and highlighted in red.

$$cos(\theta) = \overrightarrow{n_i} \cdot \overrightarrow{n_j} \rightarrow \theta = cos^{-1}(\overrightarrow{n_i} \cdot \overrightarrow{n_j}) \quad (7)$$

This approach employs the Open3D library, a commonly used library of 3D data processing available in both Python and C++ (Qian-Yi Zhou; Jaesik Park; Vladlen Koltun, 2018). Figure 39 shows an illustration of this approach on the sandblast 100 mm/min dataset.

Figure 39 – Normalization with neighboring angle verification. (a) View from above. (b) View from the side. (c) Isometric view.

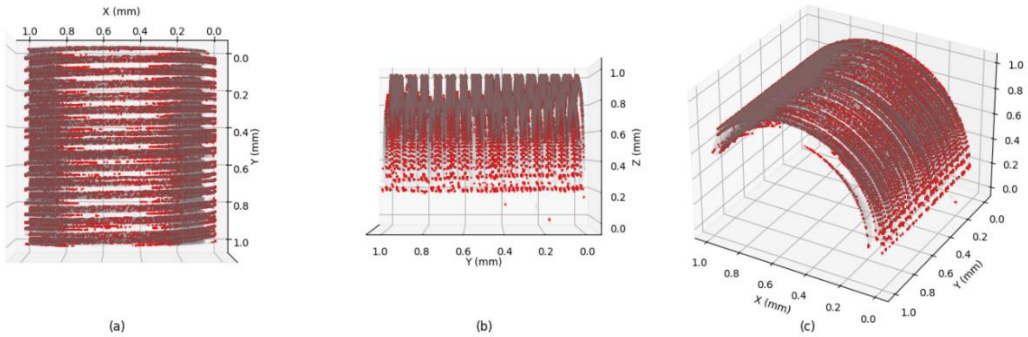

Source: Own (2025) and Fraunhofer ILT (2025).

Figure 39 displays that while many edge points are correctly identified, a great number of crevice points are also misclassified as edges compared to the first approach. Additionally, this second approach is more computationally intensive than the first one, requiring to 25,3 seconds to complete the simulation.

4.1.3 Third approach – Threshold selection

The third approach uses a more practical strategy, where it first filters the data for the script to only look between a certain threshold on the Z-axis. It then identifies the 20 most common Z-levels. This can be observed in Figure 40, where these points are highlighted in red.

Figure 40 - 20 most common Z values using sandblast 100 mm/min data

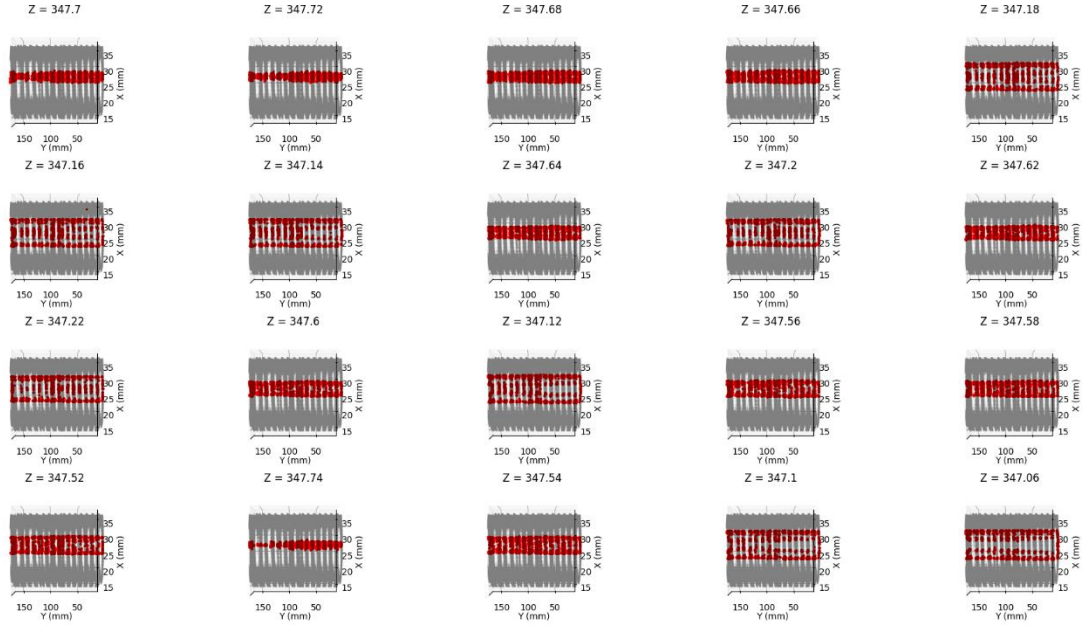

Source: Own (2025) and Fraunhofer ILT (2025).

After identifying the 20 most frequent Z-levels, as shown in Figure 40, the script processes all CSV files in the dataset, highlighting as edges (in red) only the CSV files that have values above the lowest Z-level among the 20 selected. This result is visualized in Figure 41.

Figure 41 – Threshold selection of CSV with values Z > 347.06. (a) View from above. (b) View from the side. (c) Isometric view.

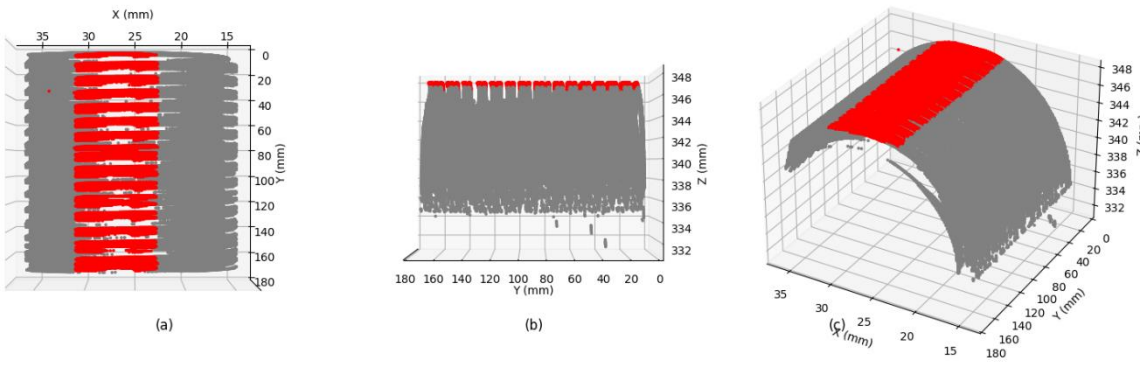

Source: Own (2025) and Fraunhofer ILT (2025).

As can be observed in Figure 41 the edges are detected with notable precision and minimal misclassification, with only a single visible point identified as an outlier. Additionally, this approach requires less computation time than the second approach (Neighboring Angles) but more when compared to the first approach (ΔZ), needing 12,3 seconds.

4.2 Considerations

Edge detection presents a problem with multiple viable solutions. In scenarios where speed and computational efficiency are critical, the preferred method should balance quick execution with accurate classification, minimizing the misidentification of edges. Among the three approaches evaluated, one demonstrated superior visual results, as illustrated in Figure 42.

Figure 42 – Visual comparison between ΔZ, Neighboring Angles, and Threshold Selection approaches with a sandblasted 100 mm/min dataset.

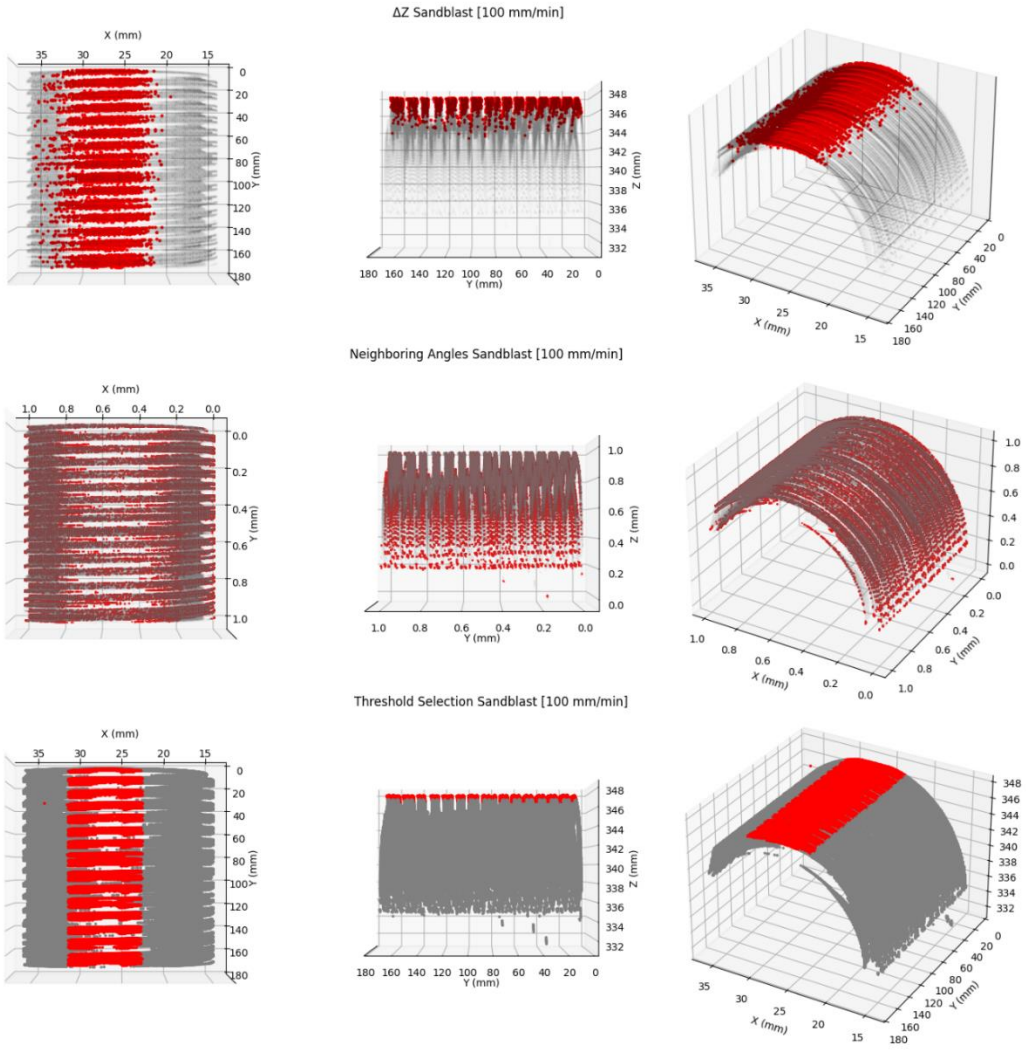

Source: Own (2025) and Fraunhofer ILT (2025).

As can be observed in Figure 42 while all three approaches detect edges, crevices are also wrongfully detected mostly in the neighboring angles approach and with some in the ΔZ approach. The threshold selection approach showed good results when detecting edges, with only one visible outlier misclassified. For the computing time it takes between each approach, Table 2 displays a comparison.

Table 2 – Simulation time taken between each approach

Edge Detection Simulations	
Description	**Simulation Time [s]**
ΔZ	3,1
Neighboring Angles	25,3
Threshold Selection	12,3

Source: Own (2025) and Fraunhofer ILT (2025).

As shown in Table 2, the ΔZ approach resulted in the fastest simulation time. However, despite its quick execution, its edge detection accuracy was surpassed by the threshold selection strategy, which took nearly four times longer to compute. Even so, this duration (12.3 seconds) represents only about one-eighth of the total scanning time (102 seconds) for a 170 mm subject scanned at 100 mm/min—demonstrating that it does not significantly impact the process efficiency. In contrast, the neighboring angles method required over eight times the computation time of the ΔZ approach and nearly double that of the threshold strategy, while delivering poorer detection results. Overall, the scripts showed good results, although considering both performance and computation time, the threshold selection method proved to be the most effective and is selected as the preferred strategy for future work.

5 FINAL CONSIDERATIONS

The increasing demand for renewable energy such as wind power has brought the attention of ensuring the reliability and efficiency of critical turbine components such as yaw and pitch control systems. Worm drives, often employed in pitch control systems, face considerable wear and degradation due to harsh environmental conditions, especially in offshore farms. This work aimed to address some of the key challenges in corrective maintenance of these pieces, which are time and finished product quality, by aiding the correction of the geometric misalignment caused by thermal expansion during the Laser Material Deposition process.

To tackle this issue, this work proposed a sensor-aided solution to detect and simulate worm drives to aid the correction of the discrepancies between the programmed and actual track position during the deposition process. A high-precision laser scanner was integrated into a CNC machine setup, enabling high-resolution data capture using a C++ developed software. Testing was then conducted using varying surface treatments and scanning speeds to optime data quality. It was found that sandblasted surfaces scanned at 100 mm/min offered the best results of the samples analyzed, with virtually no outliers.

The quality of the scanned data enabled the quick implementation and comparison of three distinct edge detection approaches: difference between neighboring points (ΔZ), surface normal angle comparison (neighboring angles), and Z-threshold selection. These methos were evaluated based on their visual accuracy, computational efficiency, and ability to distinguish gear edges from crevices. While all three approaches provided useful insights to tackle the edge detection issue, the threshold selection method stood out by delivering the most precise results with minimal false positives and a reasonable computation time. This strategy proved robust enough to serve as a foundation for future closed-loop correction systems.

From a broader perspective, this work demonstrates the feasibility of integrating sensor-based geometry monitoring with data processing algorithms to improve Laser Additive Manufacturing processes. The proposed solution can serve as a starting point for real-time feedback control systems in industrial applications such as corrective maintenance of worm drives, or any other geometry.

5.1 Future work

Although this proof of concept showed promising results for edge detection and data capture, several ways remain open for further investigation. First, the integration of this scanning system into a real-time closed loop within the CNC environment must be developed to fully automate geometric corrections, reducing both the time taken and the need for operational expertise. Second, future studies could explore machine learning-based approaches for edge and anomaly detection, potentially improving accuracy of more complex geometries sacrificing process speed. Finally, the robustness of this system should be validated on different gear geometries and surfaces, to generalize its applicability across a broader range of industrial cases.

In conclusion, the integration of sensor-based strategies with data analysis holds significant potential to ease the hurdles of corrective maintenance and repair strategies in wind energy and beyond, paving the way for more reliable and automated additive manufacturing solutions.

REFERENCES

ADEBAYO, T. S.; AWOSUSI, A. A.; BEKUN, F. V.; ALTUNTAŞ, M. Coal energy consumption beat renewable energy consumption in South Africa: Developing policy framework for sustainable development. **Renewable Energy**, v. 175. p. 1012-1024. 2021. DOI 10.1016/j.renene.2021.05.032. Available at: https://www.sciencedirect.com/science/article/pii/S0960148121007084.

ADEDOYIN, F. F.; ERUM, N.; TAŞKIN, D.; CHEBAB, D. Energy policy simulation in times of crisis: Revisiting the impact of renewable and non-renewable energy production on environmental quality in Germany. **Energy Reports**, v. 9. p. 4749-4762. 2023. DOI 10.1016/j.egyr.2023.03.120. Available at: https://www.sciencedirect.com/science/article/pii/S2352484723003578.

AHN, D.-G. Directed Energy Deposition (DED) Process: State of the Art. **Int. J. of Precis. Eng. and Manuf.-Green Tech.**, v. 8, n. 2. p. 703-742. 2021. DOI 10.1007/s40684-020-00302-7. Available at: https://link.springer.com/article/10.1007/s40684-020-00302-7?utm_source=getftr&utm_medium=getftr&utm_campaign=getftr_pilot&getft_integrator=sciencedirect_contenthosting.

AKBARI, M.; KOVACEVIC, R. Closed loop control of melt pool width in robotized laser powder–directed energy deposition process. **Int J Adv Manuf Technol**, v. 104, 5-8. p. 2887-2898. 2019. DOI 10.1007/s00170-019-04195-y. Available at: https://link.springer.com/article/10.1007/s00170-019-04195-y.

American Society for Testing and Materials. F2792-12a: Standard Terminology for Additive Manufacturing Technologies. **ASTM international.** 2012.

ANDREATTA, F. *et al.* Localized attack at inclusions in 42CrMo4 QT steel. **Electrochimica Acta**, v. 462. p. 142754. 2023. DOI 10.1016/j.electacta.2023.142754. Available at: https://www.sciencedirect.com/science/article/pii/S0013468623009325.

AREITIOAURTENA, M. *et al.* Numerical and experimental investigation of residual stresses during the induction hardening of 42CrMo4 steel. **European Journal of Mechanics - A/Solids**, v. 96. p. 104766. 2022. DOI 10.1016/j.euromechsol.2022.104766. Available at: https://www.sciencedirect.com/science/article/pii/S0997753822002029.

ARTIGAO, E.; MARTÍN-MARTÍNEZ, S.; HONRUBIA-ESCRIBANO, A.; GÓMEZ-LÁZARO, E. Wind turbine reliability: A comprehensive review towards effective condition monitoring development. **Applied Energy**, v. 228. p. 1569-1583. 2018. DOI 10.1016/j.apenergy.2018.07.037. Available at: https://www.sciencedirect.com/science/article/pii/S0306261918310651.

ASMUSSEN, M. F.; LINIGER, J.; PEDERSEN, H. C. Fault Detection and Diagnosis Methods for Fluid Power Pitch System Components—A Review. **Energies**, v. 14, n. 5. p. 1305. 2021. DOI 10.3390/en14051305. Available at: https://www.mdpi.com/1996-1073/14/5/1305.

AUGUSTYN, M. A vertical-axis rotor as the adjusting system of a horizontal axis wind turbine. **Technical Transactions.** p. 1-14. 2020. DOI 10.37705/TechTrans/e2020009.

BANFI, M.; BARALDO, S.; VANDONE, A.; VALENTE, A. Ground Control: an Acquisition and Control System Architecture for LMD. **Procedia CIRP**, v. 107. p. 605-610. 2022. DOI 10.1016/j.procir.2022.05.033. Available at: https://www.sciencedirect.com/science/article/pii/S2212827122003171.

BARALDO, S.; VANDONE, A.; VALENTE, A.; CARPANZANO, E. Closed-Loop Control by Laser Power Modulation in Direct Energy Deposition Additive Manufacturing. **Proceedings of 5th International Conference on the Industry 4.0 Model for Advanced Manufacturing.** p. 129-143. 2020. DOI 10.1007/978-3-030-46212-3_9. Available at: https://www.researchgate.net/publication/341419077_Closed-Loop_Control_by_Laser_Power_Modulation_in_Direct_Energy_Deposition_Additive_Manufacturing.

BARROS. Estratégia de Controle para Melhoramento do Comportamento Dinâmico de Turbinas Eólicas Baseadas em PMSG ligadas à Rede Elétrica**.** 2015. Available at: https://bdtd.ibict.br/vufind/Record/UFCG_f17790b60ae9acf71b81f623e0b6ae80

BEHRENS, B.-A.; BOUGUECHA, A.; BONK, C.; CHUGREEV, A. Numerical and experimental investigations of the anisotropic transformation strains during martensitic transformation in a low alloy Cr-Mo steel 42CrMo4. **Procedia Engineering**, v. 207. p. 1815-1820. 2017. DOI 10.1016/j.proeng.2017.10.944. Available at: https://www.sciencedirect.com/science/article/pii/S1877705817357375.

BERNABE, CARCEL *et al.* Improved laser metal deposition (LMD) of nickel base superalloys by pyrometry process control. p. 643-651. 2010. DOI 10.1117/12.878749. Available at: https://www.spiedigitallibrary.org/conference-proceedings-of-spie/7751/775123/Improved-laser-metal-deposition-LMD-of-nickel-base-superalloys-by/10.1117/12.878749.full.

BHARATBHAI, M. G. Failure mode and effect analysis of repower 5M wind turbine. **International Journal of Advance Research in Engineering, Science & Technology**, v. 2, n. 5. p. 7-14. 2015.

BIANCHINI, A. *et al.* Current status and grand challenges for small wind turbine technology. **Wind Energ. Sci.**, v. 7, n. 5. p. 2003-2037. 2022. DOI 10.5194/wes-7-2003-2022. Available at: https://wes.copernicus.org/articles/7/2003/2022/wes-7-2003-2022.html.

BISEROVA-TAHCHIEVA, A. *et al.* Additive Manufacturing Processes in Selected Corrosion Resistant Materials: A State of Knowledge Review. **Materials**, v. 16, n. 5. p. 1893. 2023. DOI 10.3390/ma16051893. Available at: https://www.mdpi.com/1996-1944/16/5/1893.

Bundesregierung. **Accelerated expansion of offshore wind energy | Federal Government**. *[S.l.]*, 2025. Available at: https://www.bundesregierung.de/breg-en/news/offshore-wind-energy-act-2024112. Accessed in: 22 jan. 2025.

CAI, Y.; XIONG, J.; CHEN, H.; ZHANG, G. A review of in-situ monitoring and process control system in metal-based laser additive manufacturing. **Journal of Manufacturing Systems**, v. 70. p. 309-326. 2023. DOI 10.1016/j.jmsy.2023.07.018. Available at: https://www.sciencedirect.com/science/article/pii/S0278612523001504.

CARROLL, J.; MCDONALD, A.; MCMILLAN, D. Failure rate, repair time and unscheduled O&M cost analysis of offshore wind turbines. **Wind Energy**, v. 19, n. 6. p. 1107-1119. 2016. DOI 10.1002/we.1887. Available at: https://onlinelibrary.wiley.com/doi/full/10.1002/we.1887.

CEVASCO, D.; KOUKOURA, S.; KOLIOS, A. J. Reliability, availability, maintainability data review for the identification of trends in offshore wind energy applications. **Renewable and Sustainable Energy Reviews**, v. 136. p. 110414. 2021. DOI 10.1016/j.rser.2020.110414. Available at: https://www.sciencedirect.com/science/article/pii/S1364032120307012.

CHAOUCH, D.; GUESSASMA, S.; SADOK, A. Finite Element simulation coupled to optimisation stochastic process to assess the effect of heat treatment on the mechanical properties of 42CrMo4 steel. **Materials & Design**, v. 34. p. 679-684. 2012. DOI 10.1016/j.matdes.2011.05.026. Available at: https://www.sciencedirect.com/science/article/pii/S0261306911003621.

CHEN, L. *et al.* In-situ process monitoring and adaptive quality enhancement in laser additive manufacturing: A critical review. **Journal of Manufacturing Systems**, v. 74. p. 527-574. 2024. DOI 10.1016/j.jmsy.2024.04.013. Available at: https://www.sciencedirect.com/science/article/pii/S0278612524000815.

CHEN, Y.; CHEN, Y.; LUO, W.; ZHANG, G. Development and classification of worm drive. **The 14th IFToMMWorld Congress in Taiwan**, 2015. Available at: **[Online address is missing!]**.

CHEN, Y.-J.; SHIAH, Y. Experiments on the Performance of Small Horizontal Axis Wind Turbine with Passive Pitch Control by Disk Pulley. **Energies**, v. 9, n. 5. p. 353. 2016. DOI 10.3390/en9050353. Available at: https://www.mdpi.com/1996-1073/9/5/353.

CHENG, J. *et al.* An Overview of Laser Metal Deposition for Cladding: Defect Formation Mechanisms, Defect Suppression Methods and Performance Improvements of Laser-Cladded Layers. **Materials**, v. 15, n. 16. p. 5522. 2022. DOI 10.3390/ma15165522. Available at: https://www.mdpi.com/1996-1944/15/16/5522.

COOKE, S. *et al.* Thermo-mechanical-metallurgical modelling, validation and characterization of 42CrMo4 steel processed by directed energy deposition. **Journal of Manufacturing Processes**, v. 81. p. 537-561. 2022. DOI 10.1016/j.jmapro.2022.07.007. Available at: https://www.sciencedirect.com/science/article/pii/S1526612522004753.

D D Gu; W Meiners; K Wissenbach; R Poprawe. Laser additive manufacturing of metallic components: materials, processes and mechanisms. **International Materials Reviews**, v. 57, n. 3. p. 133-164. 2012. DOI 10.1179/1743280411Y.0000000014.

DAS, P.; NANDAN, R.; PANDEY, P. M. A Review on Corrosion Properties of High Entropy Alloys Fabricated by Additive Manufacturing. **Trans Indian Inst Met**, v. 75, n. 10. p. 2465-2476. 2022. DOI 10.1007/s12666-022-02610-9. Available at: https://link.springer.com/article/10.1007/s12666-022-02610-9.

Dena Bazazian; Josep R. Casas; Javier Ruiz-Hidalgo. Fast and Robust Edge Extraction in Unorganized Point Clouds. *In*: Barros2015 International Conference on Digital Image Computing: Techniques and Applications (DICTA). **Estratégia de Controle para Melhoramento do Comportamento Dinâmico de Turbinas Eólicas Baseadas em PMSG ligadas à Rede Elétrica.**, 2015. p. 1-8. Available at: https://www.researchgate.net/publication/304288759_Fast_and_Robust_Edge_Extraction_in_Unorganized_Point_Clouds.

DONADELLO, S.; MOTTA, M.; DEMIR, A. G.; PREVITALI, B. Monitoring of laser metal deposition height by means of coaxial laser triangulation. **Optics and Lasers in Engineering**, v. 112. p. 136-144. 2019. DOI 10.1016/j.optlaseng.2018.09.012. Available at: https://www.sciencedirect.com/science/article/pii/S0143816618306675.

DONG, F. *et al.* Energy transition and carbon neutrality: Exploring the non-linear impact of renewable energy development on carbon emission efficiency in developed countries. **Resources, Conservation and Recycling**, v. 177. p. 106002. 2022. DOI 10.1016/j.resconrec.2021.106002. Available at: https://www.sciencedirect.com/science/article/pii/S092134492100611X.

ELASHA, F. *et al.* Pitting detection in worm gearboxes with vibration analysis. **Engineering Failure Analysis**, v. 42. p. 366-376. 2014. DOI 10.1016/j.engfailanal.2014.04.028. Available at: https://www.sciencedirect.com/science/article/pii/S1350630714001423.

EMEXIDIS, C.; GKONIS, P. **On the Integration of Internet of Things and Machine Learning for Energy Prediction in the Wind Turbines**. [S.l.], 2024. DOI 10.20944/preprints202409.2351.v1. Available at: https://www.researchgate.net/publication/384578111_On_the_Integration_of_Internet_of_Things_and_Machine_Learning_for_Energy_Prediction_in_the_Wind_Turbines.

FALUDI, J.; BAYLEY, C.; BHOGAL, S.; IRIBARNE, M. Comparing environmental impacts of additive manufacturing vs traditional machining via life-cycle assessment. **Rapid Prototyping Journal**, v. 21, n. 1. p. 14-33. 2015. DOI 10.1108/RPJ-07-2013-0067. Available at: https://www.emerald.com/insight/content/doi/10.1108/RPJ-07-2013-0067/full/pdf.

FANG, X. *et al.* Study on Metal Deposit in the Fused-coating Based Additive Manufacturing. **Procedia CIRP**, v. 55. p. 115-121. 2016. DOI 10.1016/j.procir.2016.08.034. Available at: https://www.sciencedirect.com/science/article/pii/S2212827116309234.

FERNANDEZ-SANCHEZ, S.; IZA-MENDIA, A.; JORGE-BADIOLA, D. Modeling Microstructure Development upon Continuous Cooling of 42CrMo4 Steel Grade for Large-Size Components. **Metals**, v. 14, n. 10. p. 1096. 2024. DOI 10.3390/met14101096. Available at: https://www.mdpi.com/2075-4701/14/10/1096#B3-metals-14-01096.

FOX, M. D. *et al.* Optical sensor to monitor and control temperature and build height of the laser direct-casting process. **Appl. Opt., AO**, v. 37, n. 36. p. 8429-8433. 1998. DOI 10.1364/AO.37.008429. Available at: https://opg.optica.org/ao/fulltext.cfm?uri=ao-37-36-8429&id=60636.

Fraunhofer ISE. **Installed Power | Energy-Charts**. *[S.l.]:* Fraunhofer ISE, 2025. Available at: **[Online address is missing!]. Accessed in:** 17 jan. 2025.

GARMENDIA, I.; LEUNDA, J.; PUJANA, J.; LAMIKIZ, A. In-process height control during laser metal deposition based on structured light 3D scanning. **Procedia CIRP**, v. 68. p. 375-380. 2018. DOI 10.1016/j.procir.2017.12.098. Available at: https://www.researchgate.net/publication/324710283_In-process_height_control_during_laser_metal_deposition_based_on_structured_light_3D_scanning.

Global Wind Energy Council. **Global Wind Report 2024**. *[S.l.]*, 2024. Available at: https://gwec.net/global-wind-report-2024/. Accessed in: 5 fev. 2025.

GONG, G. *et al.* Research status of laser additive manufacturing for metal: a review. **Journal of Materials Research and Technology**, v. 15. p. 855-884. 2021. DOI 10.1016/j.jmrt.2021.08.050. Available at: https://www.sciencedirect.com/science/article/pii/S2238785421008759.

GONZÁLEZ-BARRIO, H.; CALLEJA-OCHOA, A.; Norberto López de Lacalle, L.; LAMIKIZ, A. Hybrid manufacturing of complex components: Full methodology including laser metal deposition (LMD) module development, cladding geometry estimation and case study validation. **Mechanical Systems and Signal Processing**, v. 179. p. 109337. 2022. DOI 10.1016/j.ymssp.2022.109337. Available at: https://www.sciencedirect.com/science/article/pii/S0888327022004721.

GULPAK, M.; SÖLTER, J. Development and Validation of a Hybrid Model for the Prediction of Shape Deviations in dry Machining Processes. **Procedia CIRP**, v. 31. p. 346-351. 2015. DOI 10.1016/j.procir.2015.03.070. Available at: https://www.sciencedirect.com/science/article/pii/S2212827115003856.

GUNASEGARAM, D. R. *et al.* Machine learning-assisted in-situ adaptive strategies for the control of defects and anomalies in metal additive manufacturing. **Additive Manufacturing**, v. 81. p. 104013. 2024. DOI 10.1016/j.addma.2024.104013. Available at: https://www.sciencedirect.com/science/article/pii/S2214860424000599.

HA, K. Innovative Blade Trailing Edge Flap Design Concept using Flexible Torsion Bar and Worm Drive. **HighTech. Innov. J.**, v. 1, n. 3. p. 101-106. 2020. DOI 10.28991/HIJ-2020-01-03-01. Available at: https://hightechjournal.org/index.php/HIJ/article/view/34.

HA, K.; TRUONG, H. V. A.; DANG, T. D.; AHN, K. K. Recent Control Technologies for Floating Offshore Wind Energy System: A Review. **Int. J. of Precis. Eng. and Manuf.-Green Tech.**, v. 8, n. 1. p. 281-301. 2021. DOI 10.1007/s40684-020-00269-5. Available at: https://link.springer.com/article/10.1007/s40684-020-00269-5.

HONKALAS, R.; DESHMUKH, B.; PAWAR, P. A Review on Design and Efficiency Improvement of Worm and Worm Wheel of a Gear Motor. **J. Phys.: Conf. Ser.**, v. 1969, n. 1. p. 12023. 2021. DOI 10.1088/1742-6596/1969/1/012023. Available at: https://iopscience.iop.org/article/10.1088/1742-6596/1969/1/012023/meta.

HU, D.; KOVACEVIC, R. Sensing, modeling and control for laser-based additive manufacturing. **International Journal of Machine Tools and Manufacture**, v. 43, n. 1. p. 51-60. 2003a. DOI 10.1016/S0890-6955(02)00163-3. Available at: https://www.sciencedirect.com/science/article/pii/S0890695502001633.

HU, D.; KOVACEVIC, R. Sensing, modeling and control for laser-based additive manufacturing. **International Journal of Machine Tools and Manufacture**, v. 43, n. 1. p. 51-60. 2003b. DOI 10.1016/S0890-6955(02)00163-3. Available at: https://www.sciencedirect.com/science/article/pii/S0890695502001633.

JI, W. *et al.* Development and experimental validation of a thermo-metallurgical-mechanical model of the laser metal deposition (LMD) process. **International Journal of Pressure Vessels and Piping**, v. 211. p. 105261. 2024. DOI 10.1016/j.ijpvp.2024.105261. Available at: https://www.sciencedirect.com/science/article/pii/S0308016124001388.

JIN, X. *et al.* Failure prediction, monitoring and diagnosis methods for slewing bearings of large-scale wind turbine: A review. **Measurement**, v. 172. p. 108855. 2021. DOI 10.1016/j.measurement.2020.108855. Available at: https://www.sciencedirect.com/science/article/pii/S0263224120313464.

KANG, J.; SUN, L.; SUN, H.; WU, C. Risk assessment of floating offshore wind turbine based on correlation-FMEA. **Ocean Engineering**, v. 129. p. 382-388. 2017. DOI 10.1016/j.oceaneng.2016.11.048. Available at: https://www.sciencedirect.com/science/article/pii/S0029801816305558.

KARABACAK, Y. E.; BAŞ, H. Experimental investigation of efficiency of worm gears and modeling of power loss through artificial neural networks. **Measurement**, v. 202. p. 111756. 2022. DOI 10.1016/j.measurement.2022.111756. Available at: https://www.sciencedirect.com/science/article/pii/S0263224122009605.

KARABACAK, Y. E.; GÜRSEL ÖZMEN, N.; GÜMÜŞEL, L. Intelligent worm gearbox fault diagnosis under various working conditions using vibration, sound and thermal features. **Applied Acoustics**, v. 186. p. 108463. 2022. DOI 10.1016/j.apacoust.2021.108463. Available at: https://www.sciencedirect.com/science/article/pii/S0003682X21005570.

KIM, H.-S.; PARK, S.-H. Acoustic signal monitoring using audible cracking sounds for efficient in-situ crack detection in laser directed energy deposition of hard surfaces. **Additive Manufacturing Letters**, v. 9. p. 100210. 2024. DOI 10.1016/j.addlet.2024.100210. Available at: https://www.sciencedirect.com/science/article/pii/S2772369024000197.

KIM, S. H. Worm gear efficiency model considering misalignment in electric power steering systems. **Mech. Sci.**, v. 9, n. 1. p. 201-210. 2018. DOI 10.5194/ms-9-201-2018. Available at: https://ms.copernicus.org/articles/9/201/2018/.

Koerich. UMA PROPOSTA DE MODELO MULTICRITERIAL PARA AUXÍLIO DO PLANEJAMENTO DA MANUTENÇÃO EM AEROGERADORES: UM ESTUDO COM FOCO NA CONFIABILIDADE DE SISTEMAS ELETROMECÂNICOS. 2021.

KOMASS, T. Experimental analysis of vertical axis wind turbine active pitch control system with Permanent Magnet Synchronous Motor using MATLAB Simulink tools. **1**, v. 62, 1-2. 2016. DOI 10.6001/energetika.v62i1-2.3314. Available at: https://www.lmaleidykla.lt/ojs/index.php/energetika/article/view/3314.

KONONENKO, A. S.; IGNATKIN, I. Y.; DROZDOV, A. V. Recovering a Reducing-Gear Shaft Neck by Reinforced-Bush Adhesion. **Polym. Sci. Ser. D**, v. 15, n. 2. p. 137-142. 2022. DOI 10.1134/S1995421222020113. Available at: https://link.springer.com/article/10.1134/S1995421222020113.

KOU, L. *et al.* Review on Monitoring, Operation and Maintenance of Smart Offshore Wind Farms. **Sensors**, v. 22, n. 8. p. 2822. 2022. DOI 10.3390/s22082822. Available at: https://www.mdpi.com/1424-8220/22/8/2822.

LEE, C. *et al.* Residual stress and crack initiation in laser clad composite layer with Co-based alloy and WC + NiCr. **Applied Surface Science**, v. 345. p. 286-294. 2015. DOI 10.1016/j.apsusc.2015.03.168. Available at: https://www.sciencedirect.com/science/article/pii/S0169433215007849.

LI, F. *et al.* Point cloud data-based edge detection of precast concrete components for dimensional quality assessment using self-attention mechanisms. **Advanced Engineering Informatics**, v. 66. p. 103383. 2025. DOI 10.1016/j.aei.2025.103383. Available at: https://www.sciencedirect.com/science/article/pii/S1474034625002769.

LIM, J.-S.; OH, W.-J.; LEE, C.-M.; KIM, D.-H. Selection of effective manufacturing conditions for directed energy deposition process using machine learning methods. **Sci Rep**, v. 11, n. 1. p. 24169. 2021. DOI 10.1038/s41598-021-03622-z. Available at: https://www.nature.com/articles/s41598-021-03622-z.

LIN, Y.-C.; CHEN, M.-S.; ZHANG, J. Modeling of flow stress of 42CrMo steel under hot compression. **Materials Science and Engineering: A**, v. 499, 1-2. p. 88-92. 2009. DOI 10.1016/j.msea.2007.11.119. Available at: https://www.sciencedirect.com/science/article/pii/S0921509308006230.

LIU, Z.; ZHANG, L.; CARRASCO, J. Vibration analysis for large-scale wind turbine blade bearing fault detection with an empirical wavelet thresholding method. **Renewable Energy**, v. 146. p. 99-110. 2020. DOI 10.1016/j.renene.2019.06.094. Available at: https://www.sciencedirect.com/science/article/pii/S0960148119309334.

MACHADO. ESTRATÉGIA DE CONTROLE DE PITCH NA CAPTAÇÃO DE ENERGIA EÓLICA PARA TURBINAS OFFSHORE COM GERADOR PMSG. 2022.

MAHMOOD, M. *et al.* Laser Coatings via State-of-the-Art Additive Manufacturing: A Review. **Coatings**, v. 11, n. 3. p. 296. 2021. DOI 10.3390/coatings11030296. Available at: https://www.mdpi.com/2079-6412/11/3/296.

MathWorks. **RANSAC**. *[S.l.]*, 2025. Available at: https://www.mathworks.com/discovery/ransac.html. Accessed in: 8 mai. 2025.

Micro-Epsilon. C# Schnittstellendokumentation. 2025a. Available at: https://www.micro-epsilon.com/2d-3d-measurement/laser-profile-scanners/software/download/. Accessed in: 10 jan. 2025.

Micro-Epsilon. **scanCONTROL 29x0 | Micro-Epsilon**. *[S.l.]*, 2025b. Available at: https://www.micro-epsilon.com/2d-3d-measurement/laser-profile-scanners/scancontrol-29x0/. Accessed in: 16 mai. 2025.

MONTERO, J.; RODRÍGUEZ, Á.; AMADO, J. M.; YÁÑEZ, A. J. Inspection of Powder Flow During LMD Deposition by High Speed Imaging. **Physics Procedia**, v. 83. p. 1319-1328. 2016. DOI 10.1016/j.phpro.2016.08.139. Available at: https://www.sciencedirect.com/science/article/pii/S1875389216302462.

NAGAI, B. M.; AMEKU, K.; ROY, J. N. Performance of a 3kW wind turbine generator with variable pitch control system. **Applied Energy**, v. 86, n. 9. p. 1774-1782. 2009. DOI 10.1016/j.apenergy.2008.12.018. Available at: https://www.sciencedirect.com/science/article/pii/S0306261908003358.

NEUMANN, R.; BÖHLKE, T. Hashin–Shtrikman type mean field model for the two-scale simulation of the thermomechanical processing of steel. **International Journal of Plasticity**, v. 77. p. 1-29. 2016. DOI 10.1016/j.ijplas.2015.09.003. Available at: https://www.sciencedirect.com/science/article/pii/S0749641915001564.

NI, H.; LIN, X.; NING, X.; ZHANG, J. Edge Detection and Feature Line Tracing in 3D-Point Clouds by Analyzing Geometric Properties of Neighborhoods. **Remote Sensing**, v. 8, n. 9. p. 710. 2016. DOI 10.3390/rs8090710. Available at: https://www.mdpi.com/2072-4292/8/9/710.

NIE, M.; WANG, L. Review of Condition Monitoring and Fault Diagnosis Technologies for Wind Turbine Gearbox. **Procedia CIRP**, v. 11. p. 287-290. 2013. DOI 10.1016/j.procir.2013.07.018. Available at: https://www.sciencedirect.com/science/article/pii/S2212827113004915.

NOWOTNY, S.; SCHAREK, S.; BEYER, E.; RICHTER, K.-H. Laser Beam Build-Up Welding: Precision in Repair, Surface Cladding, and Direct 3D Metal Deposition. **J Therm Spray Tech**, v. 16, n. 3. p. 344-348. 2007. DOI 10.1007/s11666-007-9028-5. Available at: https://link.springer.com/article/10.1007/s11666-007-9028-5?utm_source=getftr&utm_medium=getftr&utm_campaign=getftr_pilot&getft_integrator=sciencedirect_contenthosting.

ONS. **Matriz de Energia Elétrica do SIN**. *[S.l.]:* Operador Nacional do Sistema, 2025. Available at: https://www.ons.org.br/paginas/sobre-o-sin/o-sistema-em-numeros. Accessed in: 16 jan. 2025.

PAN, L.; WANG, X. Variable pitch control on direct-driven PMSG for offshore wind turbine using Repetitive-TS fuzzy PID control. **Renewable Energy**, v. 159. p. 221-237. 2020. DOI 10.1016/j.renene.2020.05.093. Available at: https://www.sciencedirect.com/science/article/pii/S0960148120307916.

PAPUGA, J. *et al.* Investigation of the size effect on 42CrMo4 + QT steel in the high-cycle fatigue domain part I: Experimental campaign. **International Journal of Fatigue**, v. 175. p. 107743. 2023. DOI 10.1016/j.ijfatigue.2023.107743. Available at: https://www.sciencedirect.com/science/article/pii/S014211232300244X.

PELLIZZARI, M.; ZHAO, Z.; BOSETTI, P.; PERINI, M. Optimizing direct laser metal deposition of H13 cladding on CuBe alloy substrate. **Surface and Coatings Technology**, v. 432. p. 128084. 2022. DOI 10.1016/j.surfcoat.2022.128084. Available at: https://www.sciencedirect.com/science/article/pii/S0257897222000056.

Pengky. **Drive rod Unified Pitch Drive Mechanism | Horizontal Axis Wind Turbine | PengKy**. *[S.l.]*, 2019a. Available at: https://www.pengky.cn/zz-horizontal-axis-turbine/10-drive-rod-variable-pitch/drive-rod-variable-pitch.html. Accessed in: 9 abr. 2025.

Pengky. **Gear Unified Pitch Drive Mechanism | Horizontal Axis Wind Turbine | Pengky**. *[S.l.]*, 2019b. Available at: https://www.pengky.cn/zz-horizontal-axis-turbine/11-gear-pitch-drive-mechanism/gear-pitch-drive-mechanism.html. Accessed in: 28 jan. 2025.

Pengky. **Independent Pitch System | Horizontal Axis Wind Turbine | PengKy**. *[S.l.]*, 2019c. Available at: https://www.pengky.cn/zz-horizontal-axis-turbine/09-independent-pitch-system/independent-pitch-system.html. Accessed in: 9 abr. 2025.

Python. **GlobalInterpreterLock - Python Wiki**. *[S.l.]*, 2025. Available at: https://wiki.python.org/moin/GlobalInterpreterLock. Accessed in: 26 mai. 2025.

QI, K. *et al.* Thermal expansion control of composite coatings on 42CrMo by laser cladding. **Surface and Coatings Technology**, v. 397. p. 125983. 2020. DOI 10.1016/j.surfcoat.2020.125983. Available at: https://www.sciencedirect.com/science/article/pii/S0257897220306526.

Qian-Yi Zhou; Jaesik Park; Vladlen Koltun. Open3D: A Modern Library for 3D Data Processing. **arXiv:1801.09847.** 2018.

QIN, S.; TAO, J.; ZHAO, Z. Fault diagnosis of wind turbine pitch system based on LSTM with multi-channel attention mechanism. **Energy Reports**, v. 10. p. 4087-4096. 2023. DOI 10.1016/j.egyr.2023.10.076. Available at: https://www.sciencedirect.com/science/article/pii/S2352484723015081.

QIU, Y.; CHEN, L.; FENG, Y.; XU, Y. An Approach of Quantifying Gear Fatigue Life for Wind Turbine Gearboxes Using Supervisory Control and Data Acquisition Data. **Energies**, v. 10, n. 8. p. 1084. 2017. DOI 10.3390/en10081084. Available at: https://www.mdpi.com/1996-1073/10/8/1084#B8-energies-10-01084.

RAGHAVENDRA, S. *et al.* Process enhancements and wear evaluation of directed energy deposited bronze: Implications for reducing bronze in worm gear manufacturing. **Journal of Materials Research and Technology**, v. 34. p. 2201-2211. 2025. DOI 10.1016/j.jmrt.2024.12.242. Available at: https://www.sciencedirect.com/science/article/pii/S223878542403045X.

RANSIKARBUM, K.; PITAKASO, R.; KIM, N. A Decision-Support Model for Additive Manufacturing Scheduling Using an Integrative Analytic Hierarchy Process and Multi-Objective Optimization. **Applied Sciences**, v. 10, n. 15. p. 5159. 2020. DOI 10.3390/app10155159. Available at: https://www.mdpi.com/2076-3417/10/15/5159#B20-applsci-10-05159.

RIBRANT, J.; BERTLING, L. Survey of failures in wind power systems with focus on Swedish wind power plants during 1997-2005. **2007 IEEE Power Engineering Society General Meeting**, 2007. p. 1-8. Available at: **[Online address is missing!]**.

SCIME, L.; BEUTH, J. Using machine learning to identify in-situ melt pool signatures indicative of flaw formation in a laser powder bed fusion additive manufacturing process. **Additive Manufacturing**, v. 25. p. 151-165. 2019. DOI 10.1016/j.addma.2018.11.010. Available at: https://www.sciencedirect.com/science/article/pii/S2214860418306869.

SHIN, H.; RÜTTGERS, M.; LEE, S. Neural Networks for Improving Wind Power Efficiency: A Review. **Fluids.** 2022. DOI 10.3390/fluids7120367.

Shiyun Dong *et al.* Laser remanufacturing technology and its applications. Lasers in Material Processing and Manufacturing III: SPIE, 2008 6825). p. 381-386. Available at: https://www.spiedigitallibrary.org/conference-proceedings-of-spie/6825/68251n/laser-remanufacturing-technology-and-its-applications/10.1117/12.782335.short.

SONG, D. R. *et al.* Model Predictive Control Using Multi-Step Prediction Model for Electrical Yaw System of Horizontal-Axis Wind Turbines. **IEEE Transactions on Sustainable Energy**, v. 10, n. 4. p. 2084-2093. 2019. DOI 10.1109/TSTE.2018.2878624.

SONG, L.; BAGAVATH-SINGH, V.; DUTTA, B.; MAZUMDER, J. Control of melt pool temperature and deposition height during direct metal deposition process. **Int J Adv Manuf Technol**, v. 58, 1-4. p. 247-256. 2012. DOI 10.1007/s00170-011-3395-2. Available at: https://link.springer.com/article/10.1007/s00170-011-3395-2.

SU, H.; DONG, L.; YU, X.; LIU, K. Research on Carbon Emission for Preventive Maintenance of Wind Turbine Gearbox Based on Stochastic Differential Equation. **ENERGY**, v. 121, n. 4. p. 973-986. 2024. DOI 10.32604/ee.2023.043497. Available at: https://www.sciencedirect.com/science/article/pii/S0199859524000940.

TELLES, M. **Seis pontos importantes para a urgência da aprovação do Projeto de Lei 576/2021: Eólicas Offshore no Brasil - ABEEólica**. *[S.l.]*, 2024. Available at: https://abeeolica.org.br/seis-pontos-importantes-para-a-urgencia-da-aprovacao-do-projeto-de-lei-576-2021-eolicas-offshore-no-brasil/. Accessed in: 17 jan. 2025.

TOYSERKANI, E.; KHAJEPOUR, A. A mechatronics approach to laser powder deposition process. **Mechatronics**, v. 16, n. 10. p. 631-641. 2006. DOI 10.1016/j.mechatronics.2006.05.002. Available at: https://www.sciencedirect.com/science/article/pii/S0957415806000675.

VANDONE, A. *et al.* 3D vision system integration on Additive Manufacturing machine for in-line part inspection. **Procedia CIRP**, v. 95. p. 72-77. 2020. DOI 10.1016/j.procir.2020.01.191. Available at: https://www.sciencedirect.com/science/article/pii/S2212827120315493.

WANG, P. *et al.* The Design, Analysis, and Optimization of a New Pitch Mechanism for Small Wind Turbines. **Energies**, v. 16, n. 18. p. 6708. 2023. DOI 10.3390/en16186708. Available at: https://www.mdpi.com/1996-1073/16/18/6708.

WEI, L.; QIAN, Z.; ZAREIPOUR, H. Wind Turbine Pitch System Condition Monitoring and Fault Detection Based on Optimized Relevance Vector Machine Regression. **IEEE Transactions on Sustainable Energy**, v. 11, n. 4. p. 2326-2336. 2020. DOI 10.1109/TSTE.2019.2954834.

WHERMANN, B. **German offshore wind power - output, business and perspectives**. *[S.l.]*, 2018. Available at: https://www.cleanenergywire.org/factsheets/german-offshore-wind-power-output-business-and-perspectives. Accessed in: 22 jan. 2025.

WU, Z. *et al.* A Systematic Point Cloud Edge Detection Framework for Automatic Aircraft Skin Milling. **IEEE Transactions on Industrial Informatics**, v. 20, n. 1. p. 560-572. 2024. DOI 10.1109/TII.2023.3268404.

XIN, B. *et al.* Effect of Laser Remelting on Cladding Layer of Inconel 718 Superalloy Formed by Laser Metal Deposition. **Materials**, v. 13, n. 21. p. 4927. 2020. DOI 10.3390/ma13214927. Available at: https://www.mdpi.com/1996-1944/13/21/4927.

YIN, X.; ZHANG, W.; JIANG, Z.; PAN, L. Adaptive robust integral sliding mode pitch angle control of an electro-hydraulic servo pitch system for wind turbine. **Mechanical Systems and Signal Processing**, v. 133. p. 105704. 2019. DOI 10.1016/j.ymssp.2018.09.026. Available at: https://www.sciencedirect.com/science/article/pii/S0888327018306447.

ZHANG, C. *et al.* Improved corrosion resistance of laser melting deposited CoCrFeNi-series high-entropy alloys by Al addition. **Corrosion Science**, v. 225. p. 111599. 2023. DOI 10.1016/j.corsci.2023.111599. Available at: https://www.sciencedirect.com/science/article/pii/S0010938X23006418.

ZHANG, D.; CROSS, P.; MA, X.; LI, W. Improved control of individual blade pitch for wind turbines. **Sensors and Actuators A: Physical**, v. 198. p. 8-14. 2013. DOI 10.1016/j.sna.2013.04.020. Available at: https://www.sciencedirect.com/science/article/pii/S0924424713001842.

ZHANG, F. *et al.* Control Research on Active Pitch Control System for Horizontal-Axis Tidal-Current Turbine Generator. **Energies**, v. 18, n. 4. p. 764. 2025. DOI 10.3390/en18040764. Available at: https://www.mdpi.com/1996-1073/18/4/764.